

---

---

DISSERTATION

COLORADO STATE UNIV'S THESIS TEMPLATE

Submitted by

Matthew Gregory Hogan

Department of Physics

In partial fulfillment of the requirements

For the Degree of Doctor of Philosophy

Colorado State University

Fort Collins, Colorado

Summer 2019

Doctoral Committee:

Advisor: Walter Toki

Co-Advisor: Robert Wilson

Norman Buchanan

Wen Zhou

---

---

Copyright by Matthew Gregory Hogan 2019

---

All Rights Reserved

---

---

**ABSTRACT**

**COLORADO STATE UNIV'S THESIS TEMPLATE**

This document aims to get you started typesetting your thesis or dissertation in L<sup>A</sup>T<sub>E</sub>X.

---

---

## ACKNOWLEDGEMENTS

---

I would like to thank the Elliott Forney for making a publicly accessible L<sup>A</sup>T<sub>E</sub>X template

---



---

## TABLE OF CONTENTS

ABSTRACT . . . . .	ii
ACKNOWLEDGEMENTS . . . . .	iii
LIST OF TABLES . . . . .	vi
LIST OF FIGURES . . . . .	vii
Chapter 1 Introduction . . . . .	1
1.1 Introduction to Neutrinos . . . . .	2
1.1.1 Neutrinos in the Standard Model . . . . .	3
1.1.1.1 Weak Interactions . . . . .	5
1.1.1.2 Chirality: How Neutrinos are Left Handed . . . . .	6
1.1.1.3 Neutrino Scattering with Matter . . . . .	11
1.1.2 Neutrino Oscillations . . . . .	13
1.1.2.1 Two Flavor Derivation . . . . .	14
1.1.2.2 Three Flavor Oscillations . . . . .	18
1.1.2.2.1 Muon Neutrino Survival . . . . .	21
1.1.2.2.2 Electron Neutrino Appearance . . . . .	21
1.1.2.3 Matter Effects . . . . .	23
1.1.3 CP Violation: Origins of Matter . . . . .	24
1.2 Tokai-to-Kamioka Experiment . . . . .	25
1.2.1 Neutrino Production at J-PARC . . . . .	27
1.2.2 Neutrino Near Detectors: ND280 . . . . .	31
1.2.2.1 Multi-pixel photon counter (MPPC) . . . . .	33
1.2.2.2 On-Axis Detector . . . . .	33
1.2.2.3 Off-Axis Detector Summary . . . . .	34
1.2.2.4 Off Axis pi-zero detector (PØD) . . . . .	38
1.2.2.5 Off Axis Time Projection Chamber (TPC) . . . . .	40
1.2.2.6 Track Reconstruction in ND280 . . . . .	41
1.2.3 Neutrino Far Detector: Super-Kamiokande . . . . .	42
1.2.4 ND Constraint . . . . .	43
Chapter 2 BANFF Likelihood . . . . .	46
2.0.1 Motivation . . . . .	47
2.0.2 Introduction to Conditional PDFs and Likelihoods . . . . .	47
2.0.3 BANFF Fit Test Statistic . . . . .	48
2.0.3.1 Flux, Cross Section, and Detector Systematics . . . . .	52
Chapter 3 PØD Selections and Samples . . . . .	55
3.1 Global Reconstruction . . . . .	56
3.2 PØD Selection Cuts . . . . .	57
3.2.1 Pre-Selection Cuts . . . . .	57
3.2.2 $\nu_\mu$ CC Inclusive in FHC Cut . . . . .	60

3.2.3	$\bar{\nu}_\mu$ CC Inclusive in RHC Cuts . . . . .	61
3.2.4	$\nu_\mu$ Background CC Inclusive in RHC Cuts . . . . .	61
3.3	Selection Kinematics . . . . .	62
3.3.1	$\nu_\mu$ FHC CC 1-Track . . . . .	62
3.3.2	$\nu_\mu$ FHC CC N-Tracks . . . . .	63
3.3.3	$\bar{\nu}_\mu$ RHC CC 1-Track . . . . .	64
3.3.4	$\bar{\nu}_\mu$ RHC CC N-Tracks . . . . .	65
3.3.5	$\nu_\mu$ Background in RHC CC 1-Track . . . . .	66
3.3.6	$\nu_\mu$ RHC CC N-Tracks . . . . .	66
Chapter 4	Systematic Uncertainties . . . . .	71
4.0.1	Detector Systematic Uncertainties . . . . .	71
4.0.1.1	Efficiency-like Systematics . . . . .	71
4.0.1.2	Observable Variation Systematics . . . . .	72
4.0.1.3	Normalization Systematics . . . . .	72
Chapter 5	PØD in BANFF Parameterization . . . . .	74
5.0.1	PØD Samples Fit Binning . . . . .	74
5.0.1.1	Fit Binning Determination . . . . .	75
Chapter 6	Fitter Validation . . . . .	78
Chapter 7	Fitter Results . . . . .	79
Chapter 8	PØD and FGD BANFF Comparisons . . . . .	80
Chapter 9	Discussion . . . . .	81
Bibliography	. . . . .	82

---

---

LIST OF TABLES
----------------

1.1	Sensitivity of Different Oscillation Experiments . . . . .	19
1.2	Table of Best Fit MNSP Parameters Split by Normal and Inverted hierarchy . . . . .	23
1.3	PØD Water Target Mass Composition . . . . .	39
3.1	PØD WT FV and Corridor Definition . . . . .	59
4.1	[?] . . . . .	73

---



---

## LIST OF FIGURES

1.1	The Standard Model of particle physics . . . . .	4
1.2	CC And NC Feynman Diagrams . . . . .	6
1.3	Helicity of Neutrino Through Decay of Charged Pi Mesons . . . . .	7
1.4	$\nu_e + e^-$ Scattering . . . . .	11
1.5	Depiction of Two Neutrino Flavor Change of Basis . . . . .	16
1.6	Survival and Disappearance Probability . . . . .	17
1.7	Logarithmic Plot of the Two Flavor Survival Probability . . . . .	18
1.8	Mass hierarchy Problem And MNSP Representation . . . . .	22
1.9	Display of the matter and energy content of the Universe . . . . .	24
1.10	Birds eye view of the T2K experiment on the Japanese archipelago . . . . .	26
1.11	The T2K Unoscillated $\nu_\mu$ Flux at SK . . . . .	26
1.12	Bird's eye view of the J-PARC center . . . . .	27
1.13	Schematics of the J-PARC Accelerators . . . . .	28
1.14	The neutrino beamline at J-PARC . . . . .	29
1.15	Photographs of the Target Station . . . . .	29
1.16	T2K Accumulated Protons on Target . . . . .	30
1.17	Schematic of INGRID . . . . .	32
1.18	Photographs of the T2K MPPC . . . . .	33
1.19	INGRID Beam Profile . . . . .	34
1.20	INGRID Event Rate . . . . .	35
1.21	Schematic of the Off-Axis Near Detector ND280 . . . . .	36
1.22	ND280 Magnetic Field Deviations from a Data Fit . . . . .	37
1.23	Schematic of the PØD . . . . .	39
1.24	A cross section of a PØD scintillating bar . . . . .	40
1.25	Cut-Away Drawing of a TPC Volume in ND280 . . . . .	41
1.26	Diagram of the Super-Kamiokande Detector . . . . .	42
1.27	Representative T2K Events in Super-Kamiokande . . . . .	43
1.28	Predicted and Best Fit Measurements for the SK Flux . . . . .	44
1.29	Predicted CCInc Cross Section at T2K Energies . . . . .	45
2.1	BANFF Pre-fit Flux Covariance Matrix . . . . .	52
2.2	BANFF ND280 NuMu and ANuMu Flux Binning Parameters . . . . .	53
2.3	Cross Section Parameters Pre-fit Correlation Matrix . . . . .	53
3.1	$\nu_\mu$ FHC CC 1-Track Reconstructed Kinematics . . . . .	63
3.2	$\nu_\mu$ FHC CC 1-Track True Kinematics . . . . .	64
3.3	$\nu_\mu$ FHC CC N-Tracks Reconstructed Kinematics . . . . .	65
3.4	$\nu_\mu$ FHC CC N-Tracks True Kinematics . . . . .	66
3.5	$\bar{\nu}_\mu$ RHC CC 1-Track Reconstructed Kinematics . . . . .	67
3.6	$\bar{\nu}_\mu$ RHC CC 1-Track True Kinematics . . . . .	67

3.7	$\bar{\nu}_\mu$ RHC CC N-Tracks $P$ and $\cos\theta$ distributions broken down by true NEUT interaction modes. The top and bottom figures are water-out and water-in mode, respectively. . . . .	68
3.8	$\bar{\nu}_\mu$ in RHC CC N-Tracks $E_\nu$ , $Q^2$ , and $W$ distributions broken down by true NEUT interaction modes. . . . .	68
3.9	$\nu_\mu$ in RHC CC 1-Track $P$ and $\cos\theta$ distributions broken down by true NEUT interaction modes. The top and bottom figures are water-out and water-in mode, respectively. . . . .	69
3.10	$\nu_\mu$ in RHC CC 1-Track $E_\nu$ and $Q^2$ distributions. Sub-figure (a) is broken down by true neutrino flavor with (b) broken by more specific NEUT interaction modes. . . . .	69
3.11	$\nu_\mu$ RHC CC N-Tracks $P$ and $\cos\theta$ distributions broken down by true NEUT interaction modes. The top and bottom figures are water-out and water-in mode, respectively. . . . .	70
3.12	$\bar{\nu}_\mu$ in RHC $E_\nu$ and $Q^2$ distributions broken down by true NEUT interaction modes. . . . .	70
5.1	PØD Momenta Resolutions Used for Fit Binning . . . . .	76
5.2	PØD Angular Residuals Used for Fit Binning . . . . .	77

---

---

# Chapter 1

## Introduction

*Chose trop vue n'est chère tenue*

A thing too much seen is little prized

French proverb

---

## 1.1 Introduction to Neutrinos

The history of the neutrino can be traced back to electron energy spectrum observed in neutron  $\beta$ -decay. While measurements of  $\alpha$ - and  $\gamma$ -decay of atomic nuclei showed discrete spectral lines, the electron ( $\beta$  particle) exhibited a continuous energy spectrum. Experimentally, there were two observed particles in each decay process and classical physics dictated that the outgoing daughter particles should have discrete energies. The fact that the  $\beta$ -decay spectrum was not this way posed a fundamental problem for physicists in the mid-1910s that energy was not conserved. Two solutions were postulated: either the “energy conservation law is only valid statistically in such a process [...] or an additional undetectable new particle [...] carrying away the additional energy and spin [...] is emitted [38].” The latter solution was proposed by Wolfgang Pauli in a letter dated 4 December 1930 to a group of physicists meeting in Tübingen, modern Germany, where he first proposed the neutrino<sup>1</sup>. Pauli’s solution also predicted that the undetected neutrino would have half-integer spin, a quantum mechanical property of matter, since the observed particles in  $\beta$ -decay did not conserve angular momentum. The existence of the neutrino and validation of Pauli’s predictions would not experimentally verified for another 20 years.

The neutrino was first observed in 1953 by Clyde Cowan and Frederick Reines using a nuclear reactor in South Carolina, U.S.A.. Since then three types or “flavors” of neutrinos and antineutrinos have been observed from accelerators and also from unique sources like the Sun and a supernova. Neutrino physics continues to be an active area of physics since neutrinos are unique probes to processes otherwise inaccessible in laboratories. For instance in the depths of the Sun’s core where fusion occurs and neutrinos are created, neutrinos are

---

<sup>1</sup>In W Pauli’s December 1930 letter, he referred to his proposed particle as the “neutron”, which is not the same neutron known of today. At that point in time, the neutral particles inside the atomic nucleus, also called “neutrons”, had not been discovered, let alone understood. The neutron, which was discovered in 1932 by James Chadwick, has been formally associated as the neutral, cousin particle to the proton. It would be Enrico Fermi who would coin the particle in W Pauli’s letter and solution to the  $\beta$ -decay spectrum as a “neutrino” meaning in Italian *little neutral one*.

---

able to travel through the ultra dense and hot medium of the core (over  $10^7$  degrees Kelvin) and outer layers of the Sun and reach us on Earth.

Neutrinos rarely interact with normal matter, meaning that they travel essentially unimpeded towards one's particle detector. The rarity of such interactions can be illustrated with the fact that given nearly  $7.0 \times 10^{10}$  neutrinos/cm<sup>2</sup>/sec are incident on the Earth from the Sun<sup>2</sup>, statistically one solar neutrino can harmlessly interact with an individual in their lifetime. So this begs the question: how does one detect a neutrino? The short answer is one requires a large enough flux of neutrinos passing through a large dense volume of matter just to detect one given today's technology.

Scientists continue to be interested in neutrinos due to the unusual properties they exhibit. One of the more recent and surprising aspects about neutrinos is their ability to undergo "flavor oscillations" where a neutrino of definite flavor (type) is created and later observed as a different flavor. The impact of differences between neutrino and antineutrino oscillations could help explain the observed matter and anti-matter asymmetry in the Universe which one of the most profound mysteries in physics today.

### 1.1.1 Neutrinos in the Standard Model

The Standard Model (SM) of particle physics is the theory of elementary or fundamental particle constituents and the forces between them. These standard model forces are the electromagnetic, weak and strong. String theory, which is not yet tested, attempts to incorporate the gravitational force. The SM forces and the gravitational force constitute the four *known* fundamental forces of the Universe. Each force in the SM has at least one "force carrier" particle that mediates the interactions between particles. The force carriers are formally called "gauge bosons" which indicates they are particles with integer (0, 1, 2, ...) spin that mediate the interaction. The weak nuclear bosons, the charged  $W^\pm$  and neutral

---

<sup>2</sup>To give some perspective to this number, this means 70 billion neutrinos are traveling every second through an area similar to one's own thumb nail.

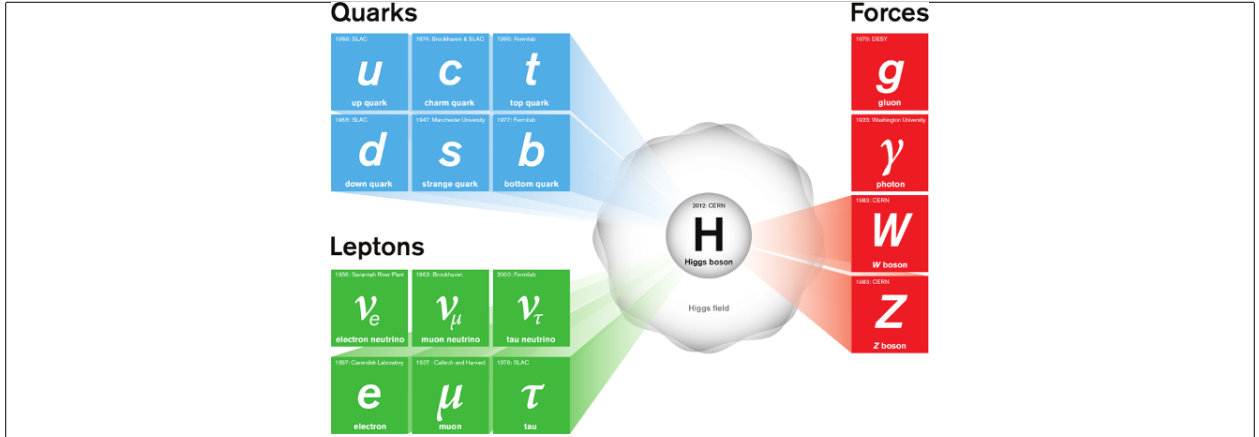


**Figure 1.1:** The Standard Model of particle physics consists of six quarks (up, down, strange, charm, bottom, and top), six leptons (electron, muon, tau, electron neutrino, muon neutrino, and tau neutrino), four force propagating bosons (gluon, photon, W, and Z), and the Higgs boson. The quarks, electron, muon, tau, W, and Z all gain mass through the Higgs field. The focus of this thesis are the neutrinos which are classified according to their charged, more massive Lepton cousins. Image taken from [7].

$Z$ , couple to neutrinos as well as the other fermions, particles with half-integer  $\left(\frac{1}{2}, \frac{3}{2}, \frac{5}{2}, \dots\right)$  spin, in the SM. All the elementary particles of the SM are shown in Figure 1.1 on page 4.

Neutrinos in the SM are electrically neutral, massless particles categorized into three generations based on their charged, more massive Lepton cousins. The neutrino and charged lepton pair into a “weak isospin doublet” in the SM. These doublets are locally gauge invariant under a  $SU(2) \times U(1)$  symmetry which leads to the postulated existence of the photon, the  $W^\pm$  and  $Z$  bosons. They are necessary to enable local gauge invariance<sup>3</sup>.

What follows is a brief introduction to weak interactions. This is followed by a exploration on the nature of neutrino handedness. Then this is proceeded by a discussion on neutrino scattering with matter.

<sup>3</sup>A gauge theory describes ways to measure physical forces or fields through interactions between elementary particles. The electric or magnetic fields for example can only be probed by charged particles. In the realm of quantum field theories, fields are postulated to permeate everywhere and it is excitations of these fields which produce experimental observables. Fields are constructed using the Lagrangian formalism and altered using gauge transformations. If altering the Lagrangian in some way does not affect the observables, this is referred to as a gauge invariance. Local gauge invariance means that under the constraints of the experiment, certain gauge transformations do not affect the observables. The allowed locally gauge invariant transformations require knowledge of its underlying Lie, or symmetry, group. With the weak isospin doublets, the Lie groups are  $SU(2) \times U(1)$  where  $SU(2)$  is the special unitary group of  $2 \times 2$  unitary matrices, and  $U(1)$  is the unitary (circle) group consisting of complex numbers of magnitude 1.

### 1.1.1.1 Weak Interactions

The name “weak force” comes from the fact that this force is much weaker than the electromagnetic and strong nuclear forces. This is due to the weak mediating bosons, the  $W^\pm$  and  $Z$ , being massive particles unlike the massless gluon ( $g$ ) and photon ( $\gamma$ ). The  $W^\pm/Z$  have masses of  $80/90 \text{ GeV}/c^2$ , which is more massive than all the elementary particles except for the top quark.

For weak interactions to occur at energies far below the masses (also called “off-shell”) of the  $W^\pm$  and  $Z$ , the interaction time must be infinitesimally small as dictated by the Heisenberg Uncertainty Principle

$$\Delta E \Delta t \gtrsim \hbar \quad (1.1)$$

where  $\Delta E$  is the energy of the particle and  $\Delta t$  is the time which the particle exists. As an example, consider a neutrino of energy of 1 GeV emitting a Z-boson of off-shell energy,  $\Delta E = 1 \text{ GeV}$  like shown in Figure 1.2 on page 6. The lifetime of that boson is about  $10^{-25} \text{ seconds}$  according to (1.1). In general, the probability that a massive particle of mass  $M$  will be created from the collision of two particles is given by a relativistic Breit–Wigner distribution

$$f(M) \propto \frac{1}{\left( (M^2 - M_0^2) c^4 \right)^2 + (M_0 c^2 \Gamma)^2}, \quad (1.2)$$

where  $M_0$  is the rest mass and  $\Gamma$  is the decay width of the particle in units of energy. For  $M \ll M_0$ , the probability of creating that particle will be infinitesimally small. Therefore to observe a single weak interaction requires a large amount of weakly interacting particles.

Weak interactions are classified into two classes of interactions: charged current (CC) and neutral current (NC). The CC interactions involve a charged W boson and change the scattering neutrino into a electrically charged lepton of flavor  $l$  where the flavor of the neutrino  $\nu_l$  is inferred from the charged lepton. The same cannot be said of NC interactions which exchange a neutral Z boson. The NC interactions are flavor agnostic since they do

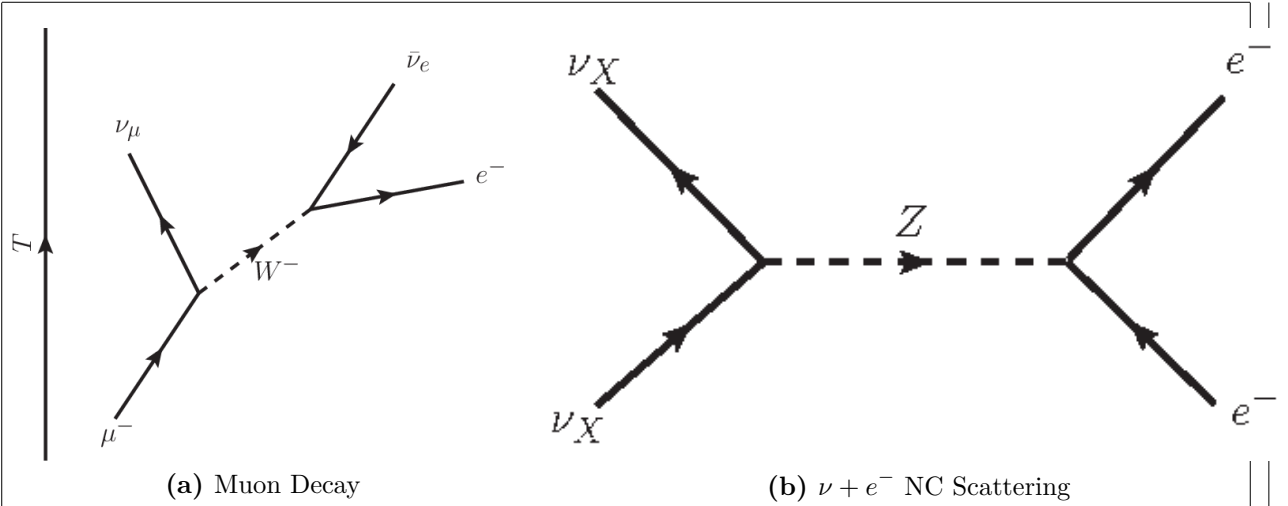


**Figure 1.2:** (a) Muon decay ( $\mu^- \rightarrow \nu_\mu \bar{\nu}_e e^-$ ) Feynman diagram with time increasing from bottom to top. This is a charged current process that converts a muon into a muon neutrino via the emission of a W boson. Due to a conserved quantum number called lepton number, the W must emit an electron and electron neutrino pair. (b) Neutral current interaction Feynman diagram where time increases from left to right. This is a neutral current interaction where a neutrino of arbitrary flavor  $X$  scatters off an electron via the emission of a Z boson.

not produce a charged lepton. An example of each interaction type is shown in Figure 1.2 on page 6.

### 1.1.1.2 Chirality: How Neutrinos are Left Handed

Neutrinos are observed to have their spin direction vectors  $\Sigma$  opposite to their momentum  $\mathbf{P}$  and this is reversed for anti-neutrinos. This property is called helicity and is given by (1.3)

$$\mathcal{H} = \frac{\Sigma \cdot \mathbf{P}}{|\mathbf{P}|}. \quad (1.3)$$

Although neutrino detection is difficult, the neutrino helicity is readily inferred from the decay of the daughter muon in the pion decay,  $\pi^\pm \rightarrow \mu^\pm + (\bar{\nu}_\mu)$ . Since a pion has net zero (0) spin, the spin vectors of the daughters must also sum to zero. The muon from a  $\pi^+$  decay has negative helicity (-1) hence the neutrino also has negative helicity. To confirm the anti-neutrino's helicity is positive (+1), the interaction requires both a charge (C) conjugation and parity (P) transformation as shown in Figure 1.3 on page 7. A C conjugation is a linear

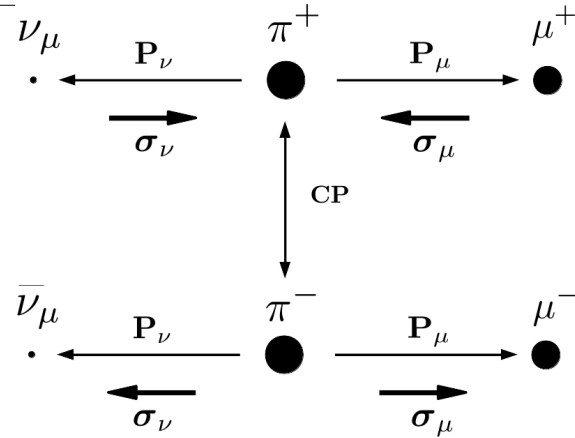


**Figure 1.3:** Decay of a charged pi meson into a muon and neutrino show the direction of the momentum  $\mathbf{P}$  and spin  $\boldsymbol{\sigma}$  of the outgoing particles. Since a pion at rest has zero (0) angular momentum, the system of daughter particles must have net zero angular momentum as well. A neutrino (antineutrino) is a right- (left-) handed helicity particle since its spin is (anti-)parallel to its momentum. Application of charge and parity (CP) converts all the particles into their respective antiparticles.

transformation that transforms all particles into their corresponding antiparticles while the  $P$  transformation inverts all spatial coordinates. Thus neutrinos are referred to *left-handed* (LH) particles while anti-neutrinos are *right-handed* (RH) particles. It turns out helicity is a useful quantum number to describe neutrinos and coincides with a property called chirality. To understand chirality and its relationship to helicity requires an analysis of the Dirac Lagrangian and Dirac equation.

The Dirac Lagrangian for a free particle field  $\psi(x)$  with half-integer spin can be written as

$$\mathcal{L} = \bar{\psi}(x) \left[ \frac{i\hbar}{2} \sum_{\mu=0}^3 \gamma^\mu (\vec{\partial}_\mu - \vec{\partial}_\mu) - mc \right] \psi(x) \quad (1.4)$$

where  $\psi(x)$  is a four-component vector (spinor) describing a particle field and  $\gamma^\mu$  are a set of four  $4 \times 4$  matrices. The adjoint field  $\bar{\psi}(x)$  is defined as

$$\bar{\psi}(x) \equiv \psi^\dagger(x) \gamma^0 \quad (1.5)$$

where  $\dagger$  denotes the conjugate and transpose operations. The  $\overrightarrow{\partial}_\mu$  operator is a four-vector defined as

$$\partial_0 = \frac{1}{c} \frac{\partial}{\partial t}, \partial_1 = \frac{\partial}{\partial x}, \partial_2 = \frac{\partial}{\partial y}, \partial_3 = \frac{\partial}{\partial z} \quad (1.6)$$

that acts only on the right of it while  $\overleftarrow{\partial}_\mu$  only acts on its left (i.e.  $\overline{\psi} \overleftarrow{\partial}_\mu = \partial_\mu \overline{\psi}$ ). The  $\gamma^\mu$  matrices are not unique and different representations dictate different kinematic regimes.

The field equations are extracted from the Lagrangian using the Euler-Lagrange procedure. In general for a set of  $M$  fields, the field equation are given by

$$\partial_\mu \frac{\partial \mathcal{L}}{\partial (\partial_\mu \psi_r)} - \frac{\partial \mathcal{L}}{\partial \psi_r} = 0 \quad (r = 0, 1, 2, \dots, M-1, M). \quad (1.7)$$

For the Dirac Lagrangian, the field equation for  $\psi$  is given by

$$\partial_\mu \frac{\partial \mathcal{L}}{\partial (\partial_\mu \overline{\psi})} - \frac{\partial \mathcal{L}}{\partial \overline{\psi}} = 0 \quad (1.8)$$

which yields the Dirac equation

$$\left[ i\hbar \sum_{\mu=0}^3 \gamma^\mu \partial_\mu - mc \right] \psi(x) = 0. \quad (1.9)$$

The representation of the  $\gamma^\mu$  matrices that is useful to describe neutrinos is the *Chiral representation* (also called the *Weyl representation*) where

$$\gamma^0 = \begin{bmatrix} 0 & I_2 \\ -I_2 & 0 \end{bmatrix}, \gamma^1 = \begin{bmatrix} 0 & \sigma_x \\ -\sigma_x & 0 \end{bmatrix}, \gamma^2 = \begin{bmatrix} 0 & \sigma_y \\ -\sigma_y & 0 \end{bmatrix}, \gamma^3 = \begin{bmatrix} 0 & \sigma_z \\ -\sigma_z & 0 \end{bmatrix}, \quad (1.10)$$

$I_2$  is the  $2 \times 2$  identity matrix,  $\sigma_{x,y,z}$  are the Pauli Spin matrices given by

$$\sigma_x = \sigma_1 = \begin{pmatrix} 0 & 1 \\ 1 & 0 \end{pmatrix}, \quad \sigma_y = \sigma_2 = \begin{pmatrix} 0 & -i \\ i & 0 \end{pmatrix}, \quad \sigma_z = \sigma_3 = \begin{pmatrix} 1 & 0 \\ 0 & -1 \end{pmatrix}.$$

---

Using the Chiral representation, the chirality matrix,  $\gamma^5$  (the fifth gamma matrix), is defined as

$$\gamma^5 = i\gamma^0\gamma^1\gamma^2\gamma^3 = \begin{bmatrix} I_2 & 0 \\ 0 & -I_2 \end{bmatrix}, \quad (1.11)$$

which is diagonal as well as Hermitian meaning that its eigenvalues are real and observable.

Let eigenfunctions of the chirality matrix be denoted with subscripts  $P$  and  $M$  such that the eigenvalue equations are

$$\begin{aligned} \gamma^5\psi_P &= +1\psi_P, \\ \gamma^5\psi_M &= -1\psi_M. \end{aligned} \quad (1.12)$$

The field equation solutions to (1.9) can be decomposed into  $\psi_P$  and  $\psi_M$  projections using two chiral projection operators  $\hat{O}_{P,M}$  where

$$\psi = (\hat{O}_P + \hat{O}_M)\psi = \psi_P + \psi_M. \quad (1.13)$$

The chiral operators are explicitly given by

$$\begin{aligned} \hat{O}_M &= \frac{1}{2}(I_4 - \gamma^5) = \begin{pmatrix} 0 & 0 \\ 0 & I_2 \end{pmatrix}, \\ \hat{O}_P &= \frac{1}{2}(I_4 + \gamma^5) = \begin{pmatrix} I_2 & 0 \\ 0 & 0 \end{pmatrix}, \end{aligned} \quad (1.14)$$

where  $I_4$  is the  $4 \times 4$  identity matrix. Taken together (1.13) and (1.14) indicate the free neutrino field is a vector  $\psi$  minus axial vector  $\gamma^5\psi$ , also referred to as V-A, under P transformations. This feature is what allows for the weak force to violate P-symmetry and CP-symmetry. Referring back to (1.4) and (1.7), the Dirac equation becomes a set of coupled equations

---

$$\begin{aligned} i\hbar \sum_{\mu=0}^3 \gamma^\mu \partial_\mu \psi_P &= mc\psi_M, \\ i\hbar \sum_{\mu=0}^3 \gamma^\mu \partial_\mu \psi_M &= mc\psi_P \end{aligned} \tag{1.15}$$

where dynamics are set by the mass.

Since the chiral projection operators are decompositions of the identity matrix, the simplest nontrivial solution to  $\psi$  is

$$\psi = \begin{pmatrix} \chi_P \\ \chi_M \end{pmatrix} \tag{1.16}$$

where  $\chi$  represent two-component spinors. Using 1.16 the Dirac equation in (1.15) can again be rewritten as

$$\begin{aligned} i\hbar \left[ \frac{1}{c} \frac{\partial}{\partial t} + \boldsymbol{\sigma} \cdot \boldsymbol{\nabla} \right] \chi_P &= -mc\chi_M, \\ i\hbar \left[ \frac{1}{c} \frac{\partial}{\partial t} - \boldsymbol{\sigma} \cdot \boldsymbol{\nabla} \right] \chi_M &= -mc\chi_P, \end{aligned} \tag{1.17}$$

where

$$\boldsymbol{\sigma} \cdot \boldsymbol{\nabla} = \sigma_x \frac{\partial}{\partial x} + \sigma_y \frac{\partial}{\partial y} + \sigma_z \frac{\partial}{\partial z}. \tag{1.18}$$

In the limiting case of vanishing mass ( $m \rightarrow 0$ ), as is in the SM, the free particle field equations in (1.17) decouple into

$$\begin{aligned} \left( \frac{E}{c} + \boldsymbol{\sigma} \cdot \boldsymbol{P} \right) \chi_P &= 0, \\ \left( \frac{E}{c} - \boldsymbol{\sigma} \cdot \boldsymbol{P} \right) \chi_M &= 0, \end{aligned} \tag{1.19}$$

where the differential operators have been evaluated as the particle's energy  $E$  and momentum three-vector  $\boldsymbol{P}$ . For massless neutrinos,  $\chi_P$  and hence  $\psi_P$ , describe particles of negative energy  $E = -|\boldsymbol{P}|c$  which in the context of quantum field theory are interpreted as antiparticles traveling backwards in time. Conversely,  $\psi_M$  have positive energy  $E = |\boldsymbol{P}|c$  and which means they are particles traveling forward in time.

If one also multiplies (1.15) by  $\gamma^5 \gamma^0$  and using the fact that the spin operator  $\boldsymbol{\Sigma}$  is

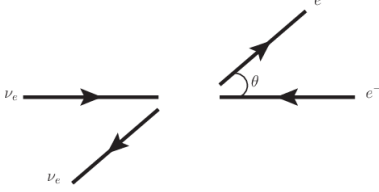


**Figure 1.4:** The definition of  $\theta$  in  $\nu_e + e^-$  (shown) and  $\bar{\nu}_e + e^-$  (not shown) scattering.

$$\Sigma = i(\gamma^2\gamma^3, \gamma^3\gamma^1, \gamma^1\gamma^2) = \gamma^0\gamma^k\gamma^5 \quad (k = 1, 2, 3) \quad (1.20)$$

each decoupled equation becomes

$$\frac{\Sigma \cdot \mathbf{P}}{|\mathbf{P}|} \psi_{P,M} = \gamma^5 \psi_{P,M} = \pm \psi_{P,M}, \quad (1.21)$$

where one recognizes that helicity and chiral states are the same for  $m \rightarrow 0$  only. Thus the labels  $M$  and  $P$  actually are identical to the LH and RH helicity labels, respectively. Using the results on helicity from before, a neutrino is always observed as a LH particle while the anti-neutrino is always observed as a RH antiparticle.

The observation of only LH neutrinos and RH anti-neutrinos is an important feature in the SM. However, since neutrinos are known to have mass from oscillations, it is theoretically possible to observe a RH neutrino and LH anti-neutrino. That would require boosting to a highly relativistic reference frame with respect to the laboratory.

### 1.1.1.3 Neutrino Scattering with Matter

Charged current (CC) neutrino interactions on nuclear particles are the interactions used in this thesis. These interactions produce an outgoing charged lepton and a variety of hadronic states. While interactions with valence electrons is possible, they are far less common in large, subatomic particle detectors. However, the physics of neutrino-electron scattering is very similar to neutrino-nucleus scattering.

Consider neutrino-electron scattering, the cross section for  $\nu_e + e^-$  is given by

$$\frac{d\sigma}{d\Omega} = \left(\frac{G\hbar c}{2\pi}\right)^2 s, \quad (1.22)$$

where  $G$  is the Fermi constant and  $s$  is the center of mass energy squared. Due to the V-A nature of the Weak force, neutrinos couple to LH particles and RH antiparticles. The outgoing particles are isotropically distributed in the center-of-mass frame since the initial and final spin state of the system is  $J = 0$ . Compare equation (??) with the cross section for  $\bar{\nu}_e + e^-$

$$\frac{d\sigma}{d\Omega} = \left(\frac{G\hbar c}{4\pi}\right)^2 (1 - \cos\theta)^2 s, \quad (1.23)$$

where  $\theta$  is the observed scattering angle of the electron as shown in Figure 1.4 on page 11. Since the total spin of the  $\bar{\nu}_e + e^-$  system is  $J = 1$  with z-projection  $J_z = 1$ , the antineutrino is preferentially forward scattered. Integrating over all angles, the cross sections come out to

$$\sigma(\bar{\nu}_e + e^-) = \frac{1}{3} \sigma(\nu_e + e^-).$$

The factor  $1/3$  arises from the fact that angular momentum conservation forbids the  $J_z = -1$  and  $0$  states for  $\bar{\nu}_e + e^-$  scattering. The same  $1/3$  factor arises between  $\nu_\mu + d \rightarrow \mu^- + u$  and  $\bar{\nu}_\mu + u \rightarrow \mu^+ + d$  scattering.

In neutrino-nuclear scattering, the simple picture of free quarks must be replaced with the reality of the nuclear medium. Interactions with a single quark are still possible, but nuclear effects can alter the products of the interactions. The kinematics of the particles involved can be altered as well as the existence of a particle can be change depending on the point of interaction. Distinctions must be made in neutrino physics between point-like interactions ( $\nu_e + e^-$ ) and post “final state interactions” (FSI) are what is actually observable in an experiment.

Neutrino-nuclear scattering presented in this thesis come in three primary CC varieties: quasi-elastic (CCQE), deep inelastic scattering (CCDIS), and single pion production (CC1 $\pi$ ). CCQE interactions refer to the process where an incoming neutrino (antineutrino) and neu-

---

tron (proton) produce a charged lepton and proton (neutron). This process is thought of classically to have approximate mass conservation between the proton-neutron states ( $\Delta m = 1.29 \text{ MeV}/c^2$ ). The CCQE interactions are the lowest energy CC interaction with a nucleon. While CCQE models work well for low-Z atoms like hydrogen, they do not extend well into many nucleon atoms. CCDIS is a high energy transfer process that shatters the nucleus apart which has the observation of many post-FSI hadrons. Modeling CCDIS can be challenging due to FSI and the uncertainty of the possible initial states of the nucleus. Finally CC $1\pi$  interactions refer to processes where a post-FSI charged pion is experimentally observed presumably from the decay of resonance state like the  $\Delta(1232)$  baryon. These interactions are not well understood currently since they occur in the transition between CCQE and CCDIS interaction modes.

### 1.1.2 Neutrino Oscillations

Neutrino oscillations are the observation of a neutrino produced with a particular, definite flavor and later observed as a different flavor. This phenomenon was first observed as a deficit of neutrinos for a number of atmospheric and solar neutrino experiments. The deficit also seemed more pronounced for atmospheric neutrinos as the distance from their source increased. For neutrino oscillations to occur, at least one neutrino must be massive. This observation firmly established that the SM is wrong with its assumption of massless neutrinos.

The first indication of neutrino oscillations was from the Ray Davis Homestake Mine experiment [13]which began in the 1960s. Ray Davis was an expert chemist and designed a radiochemical experiment to measure the flux of neutrinos from Sun. The purpose of this experiment was to test John Bahcall's prediction of the fusion rate in the Sun and neutrino flux from it as well. Davis' experiment would need to operate for many years to collect enough statistics due to expected low capture rate. Measurements continued into the 1980s and showed that the flux of neutrinos as measured at Homestake and this was about  $1/3$

---

the expected rate and this became known as the “Solar Neutrino Problem.” The primary solutions were either the solar model was incorrect or the neutrino capture cross section was incorrect. The Sudbury Neutrino Observatory (SNO) was able to resolve this problem by making a model-independent measurement of the solar neutrino flux. SNO observed a  $\nu_e$  CC-to-NC ratio of  $0.301 \pm 0.033$ , which confirmed that only about 30% of neutrinos arrive as  $\nu_e$  flavors on Earth. Saying this another way, the majority of neutrinos arrive as the wrong flavor [38].

Another outstanding problem emerged with measurements of atmospheric neutrinos, in particular muon and electron types. Atmospheric neutrinos are produced when high energy cosmic rays strike atmospheric particles. These cosmic ray collisions generate mostly pions and kaons that decay into neutrinos. When trying to measure the  $\nu_\mu/\nu_e$  ratio and comparing that with expected ratio, there was another significant deficit. This was particularly a problem as a function of the zenith angle for the Super-Kamiokande (SK) experiment. SK is a 50kt tank of pure water lined with thousands of photomultiplier tubes designed to observe solar and atmospheric neutrinos. It was the first experiment to perform a neutrino oscillation analysis that successfully explained the deficit.

The observation of neutrino oscillations is relatively new, or about three decades old. Bruno Pontecorvo [28] first proposed such a mechanism in 1957 between neutrinos and antineutrinos much like known neutral K-mesons oscillations. However, oscillations between flavored neutrinos was not expected since it requires the neutrino to have mass. The reasons why are explained in the next subsection.

### 1.1.2.1 Two Flavor Derivation

The phenomenon of neutrino oscillations can be described with elementary, non-relativistic Quantum Mechanics. Beginning with the Schrödinger Equation in (1.24)

$$-\frac{\hbar}{i} \frac{d}{dt} |\nu(\mathbf{r}, t)\rangle = \hat{H} |\nu(\mathbf{r}, t)\rangle, \quad (1.24)$$

---

where  $\hat{H}$  is the Hamiltonian for the physical system, one considers a massive neutrino of mass  $m_j$  in its rest frame (free particle). The Hamiltonian is diagonal in this case, which acting on  $|\nu_j\rangle$  results in the eigenvalue equation

$$\hat{H} |\nu_j(\mathbf{r}, t)\rangle = E_j |\nu_j(\mathbf{r}, t)\rangle, \quad (1.25)$$

where  $E_j$  is the energy of the neutrino  $|\nu_j\rangle$ . Substituting (1.25) into (1.24) and solving for  $|\nu(\mathbf{r}, t)\rangle$ , one obtains the following

$$|\nu_j(\mathbf{r}, t)\rangle = e^{-iE_j t/\hbar} |\nu_j(\mathbf{r}, t=0)\rangle, \quad (1.26)$$

where  $|\nu_j(\mathbf{r}, t=0)\rangle$  is created with momentum  $\mathbf{p}$  at the origin  $\mathbf{r} = 0$ . The time-independent solution to (1.24) is a plane-wave given by

$$|\nu_j(\mathbf{r}, t=0)\rangle = e^{i\mathbf{p} \cdot \mathbf{r}/\hbar} |\nu_j\rangle. \quad (1.27)$$

Before being able to describe neutrino oscillations, the basis states must be defined. For this example, consider that there are only two eigenstates, labeled  $\nu_1$  and  $\nu_2$ , in the “mass” basis with definite mass  $m_1$  and  $m_2$ , respectively. However, experiments can produce neutrinos, as well as probe them, only in a definite flavor state, denoted by a Greek letter subscript  $\lambda$ . Let the generated neutrino, which is a linear superposition of mass states 1 and 2, have momentum  $\mathbf{p}$  and flavor  $\alpha$ . Since both mass eigenstates share the same momentum momentum  $\mathbf{p}$  (but not energy!), the exponential term in (1.27) is an overall phase that will cancel out later. One can postulate a linear transformation,  $U$ , between the basis states given by (1.28).

$$\begin{bmatrix} \nu_\alpha \\ \nu_\beta \end{bmatrix} = \begin{bmatrix} U_{11} & U_{12} \\ U_{21} & U_{22} \end{bmatrix} \begin{bmatrix} \nu_1 \\ \nu_2 \end{bmatrix} \quad (1.28)$$

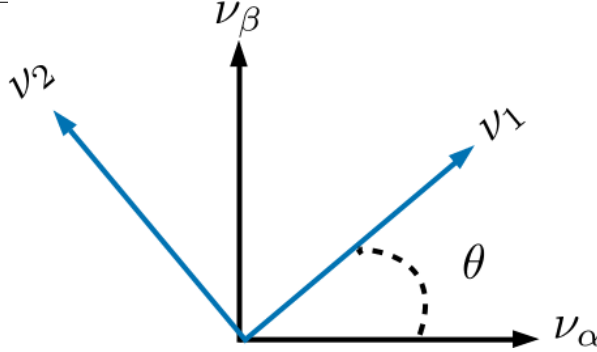


**Figure 1.5:** The depiction of two neutrino flavor change of basis using a rotation matrix. Compare this with equation (??).

This linear transformation must be a unitary matrix ( $U^{-1} = U^\dagger$ ,  $\dagger$  = transpose conjugate) since the states  $\nu_{1,2}$  constitute a complete orthonormal basis in the mass basis. With this unitary property,  $U$  can be written as a rotation matrix

$$\begin{bmatrix} \nu_\alpha \\ \nu_\beta \end{bmatrix} = \begin{bmatrix} \cos(\theta) & \sin(\theta) \\ -\sin(\theta) & \cos(\theta) \end{bmatrix} \begin{bmatrix} \nu_1 \\ \nu_2 \end{bmatrix}, \quad (1.29)$$

where  $\theta$  is the angle between the two bases. One can imagine this transformation between bases as shown in Figure 1.5 on page 16 . Creating a neutrino of flavor  $\alpha$  and observe it after a time  $t = T > 0$ , the probability of observing it as flavor  $\beta \neq \alpha$  is given by

$$\begin{aligned} \mathcal{P}(\nu_\alpha \rightarrow \nu_\beta) &= |\langle \nu_\alpha(t=0) | \nu_\beta(t=T) \rangle|^2 \\ &= |\{\cos(\theta) \langle \nu_1(t=0) | + \sin(\theta) \langle \nu_2(t=0) | \} \\ &\quad \times \{-\sin(\theta) |\nu_1(t=T)\rangle + \cos(\theta) |\nu_2(t=T)\rangle\}|^2. \end{aligned} \quad (1.30)$$

Evaluating all inner products and simplifying terms in (1.30) results in (1.31) below.

$$\mathcal{P}(\nu_\alpha \rightarrow \nu_\beta) = \sin^2(2\theta) \sin^2\left(\frac{E_1 - E_2}{2\hbar}T\right) \quad (1.31)$$

The terminology of “neutrino oscillations” should be more apparent now since (1.31) demonstrates that the probability changes sinusoidally as a function of time  $T$ . This equa-

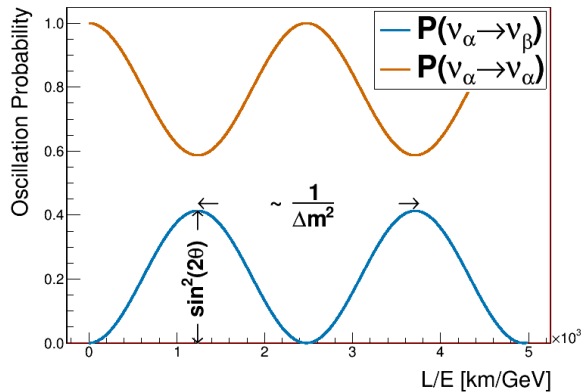


**Figure 1.6:** Two flavor oscillation probability as a function  $L/E$  is shown using  $\theta = 20^\circ$  and  $\Delta m^2 = 10^{-3} \text{ eV}^2/c^4$ . The spacing between adjacent peaks/troughs is proportional to the inverse of  $\Delta m^2$ . Note that  $\mathcal{P}(\nu_\alpha \rightarrow \nu_\alpha) = 1 - \mathcal{P}(\nu_\alpha \rightarrow \nu_\beta)$  since the oscillation probability must always sum to 1.

tion is not, however, terribly useful in the laboratory frame since it is hard to design an experiment where the travel time an individual neutrino is well known. Instead, one can make useful approximations that are accessible in the laboratory frame. Since neutrinos are nearly massless, they travel very close to the speed of light. Therefore time  $T$  is replaced with  $L/c$  where  $L$  is the distance between the neutrino origin and detection and  $c$  is now the speed of light in vacuum. One can also approximate the energy of the mass eigenstate as

$$\begin{aligned} E_j &= \left( m_j^2 c^4 + p_j^2 c^2 \right)^{\frac{1}{2}} = p_j c \left( 1 + \frac{m_j^2 c^2}{p_j^2} \right)^{\frac{1}{2}} \\ &\approx p_j c \left( 1 + \frac{m_j^2 c^2}{2p_j^2} + \mathcal{O} \left( \frac{m_j c}{p_j} \right)^4 \right) \\ &\approx E_\nu + \frac{m_j^2 c^4}{2E_\nu}, \end{aligned} \quad (1.32)$$

where for oscillation experiments  $p_j \gg m_j c$  and  $p_j \approx E_\nu$  where  $E_\nu$  is the neutrino energy as measured in the laboratory. Substituting these assumptions in (1.31), the oscillation probability is given by

$$\mathcal{P}(\nu_\alpha \rightarrow \nu_\beta) = \sin^2(2\theta) \sin^2 \left( \frac{\Delta m^2 c^3}{4\hbar} \frac{L}{E_\nu} \right), \quad (1.33)$$

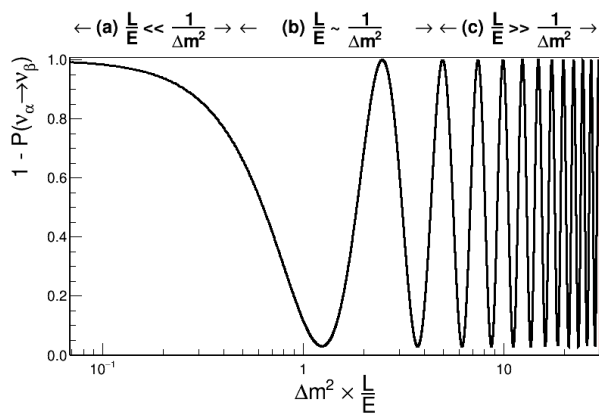


**Figure 1.7:** Logarithmic plot of the survival probability of flavor  $\alpha$  ( $1 - \mathcal{P}(\nu_\alpha \rightarrow \nu_\beta) = \mathcal{P}(\nu_\alpha \rightarrow \nu_\alpha)$ ) over a wide range of  $L/E$  values for  $\theta = 40^\circ$ . The arrows above the plot very roughly denote three possible cases: (a) no oscillations ( $L/E \ll 1/\Delta m^2$ ); (b) sensitivity to oscillations ( $L/E \sim 1/\Delta m^2$ ); (c) only average measurement ( $L/E \gg 1/\Delta m^2$ ). Image originally inspired by [32].

where  $\Delta m^2 = m_2^2 - m_1^2$  is the mass-squared difference between the mass states. For a momentum consider evaluating all the physical constants in natural units ( $c = \hbar = 1$ ). An appropriate choice of units for  $\Delta m^2$ ,  $L$ , and  $E_\nu$  results in

$$\mathcal{P}(\nu_\alpha \rightarrow \nu_\beta) = \sin^2(2\theta) \sin^2 \left( 1.27 \frac{\Delta m^2}{[\text{eV}^2]} \frac{L/E_\nu}{[\text{km}/\text{GeV}]} \right) \text{ [natural units]} \quad (1.34)$$

which more clearly demonstrates the Physics in neutrino oscillations. The oscillation probability has an amplitude of  $\sin^2(2\theta)$  and varies with frequency inversely proportional to  $\Delta m^2$  as illustrated in Figure 1.6 on page 17. Since  $L$  and  $E_\nu$  are the only controllable parameters for an oscillation experiment, probing  $\theta$  or  $\Delta m^2$  can be difficult unless the experiment can probe a large range of  $L/E_\nu$ , as shown in Figure 1.7 on page 18.

### 1.1.2.2 Three Flavor Oscillations

In the general case of oscillations using a  $n \times n$  mixing matrix, the unitary transformation can be written as a rotation matrix with  $\frac{n}{2}(n-1)$  weak mixing angles with  $\frac{1}{2}(n-2)(n-1)$  Charge-Parity (CP) violating phases. In addition, oscillations are dictated by a total of  $n-1$  mass-squared splittings [38]. This all assumes that neutrinos obey the Dirac Equation, or

Source	Species	Baseline [km]	Mean Energy [GeV]	$\min(\Delta m^2)$ [eV $^2$ ]
Reactor	$\bar{\nu}_e$	1	$\sim 10^{-3}$	$\sim 10^{-3}$
Reactor	$\bar{\nu}_e$	100	$\sim 10^{-3}$	$\sim 10^{-5}$
Accelerator	$\nu_\mu, \bar{\nu}_\mu$	1	$\sim 1$	$\sim 1$
Accelerator	$\nu_\mu, \bar{\nu}_\mu$	$10^3$	$\sim 1$	$\sim 10^{-3}$
Atmospheric $\nu$ 's	$\nu_{e,\mu}, \bar{\nu}_{\mu,e}$	$10^4$	$\sim 1$	$\sim 10^{-4}$
Sun	$\nu_e$	$1.5 \times 10^8$	$\sim 10^{-3}$	$\sim 10^{-11}$

**Table 1.1:** Sensitivity of different oscillation experiments originally published in [34].

that they are not their own antiparticles. The favored mixing model is the  $3 \times 3$  matrix since there are three known neutrino flavors,  $\nu_e$ ,  $\nu_\mu$ , and  $\nu_\tau$ . This means that there are three (3) mixing angles, one (1) CP violating phase, and three (3) mass-squared splittings.

The most frequently used matrix parameterization is the MNSP (MNSP: Maki-Nakagawa-Sakata-Pontecorvo) matrix. Pontecorvo is accredited for first conceiving of neutrino oscillations, albeit between neutrino and anti-neutrinos [27]. It was Maki, Nakagawa, and Sakata who conceived of the parameterization based off the ideas of Pontecorvo [26]. The MNSP matrix is decomposed into separate rotation matrices as given by (1.35)

$$U_{\text{MNSP}} = \underbrace{\begin{bmatrix} 1 & 0 & 0 \\ 0 & c_{32} & s_{32} \\ 0 & -s_{32} & c_{32} \end{bmatrix}}_{U_{32}=U_{\text{atm}}} \times \underbrace{\begin{bmatrix} c_{31} & 0 & s_{31}e^{i\delta_{\text{CP}}} \\ 0 & 1 & 0 \\ -s_{31}e^{-i\delta_{\text{CP}}} & 0 & c_{31} \end{bmatrix}}_{U_{31}=U_{\text{rea}}} \times \underbrace{\begin{bmatrix} c_{21} & s_{21} & 0 \\ -s_{21} & c_{21} & 0 \\ 0 & 0 & 1 \end{bmatrix}}_{U_{21}=U_{\text{sol}}}, \quad (1.35)$$

where

$$c_{ij} = \cos \theta_{ij}, \quad s_{ij} = \sin \theta_{ij}, \quad (1.36)$$

and  $\delta_{\text{CP}}$  represents the CP violating phase. Each rotation matrix  $U_{ij}$  represents the different sources for neutrino oscillations experiments with “atm”, “rea”, and “sol” representing atmospheric  $\nu$ 's, nuclear reactor  $\nu$ 's, and Solar  $\nu$ 's, respectively. The sensitivity of neutrino oscillations for different sources is given in Table 1.1 on page 19.

If neutrinos are their own antiparticles, they do not follow the Dirac Equation but do follow the Majorana Equation. This adds two (in general  $n - 1$ ) more CP violating Majorana phases,  $\alpha$  and  $\beta$ , to the MNSP matrix

$$U_{\text{MNSP}} \rightarrow U_{\text{MNSP}} \times \overbrace{\begin{bmatrix} 1 & 0 & 0 \\ 0 & e^{i\alpha} & 0 \\ 0 & 0 & e^{i\beta} \end{bmatrix}}^{\text{U}_{\text{Majorana}}} . \quad (1.37)$$

Unfortunately, neutrino oscillations are not able to probe the Majorana phases since the Majorana matrix is diagonal. The question of if neutrinos are Majorana ( $\nu = \bar{\nu}$ ) or Dirac ( $\nu \neq \bar{\nu}$ ) particles is an open question and is being explored by neutrinoless double beta decay experiments [31].

The full three flavor oscillation probability is given by

$$\begin{aligned} \mathcal{P}(\nu_\alpha \rightarrow \nu_\beta) = & \delta_{\alpha\beta} - 4 \sum_{j=1}^3 \left[ \sum_{i>j}^3 \text{Re}(K_{\alpha\beta,ij}) \sin^2(\phi_{ij}) \right] \\ & + 4 \sum_{j=1}^3 \left[ \sum_{i>j}^3 \text{Im}(K_{\alpha\beta,ij}) \sin(\phi_{ij}) \cos(\phi_{ij}) \right] \end{aligned} \quad (1.38)$$

where

$$K_{\alpha\beta,ij} = U_{\alpha i} U_{\beta i}^* U_{\alpha j}^* U_{\beta j} \quad (1.39)$$

encapsulates the MNSP matrix elements and

$$\phi_{ij} = \frac{\Delta m_{ij}^2 c^3}{4\hbar} \frac{L}{E_\nu}. \quad (1.40)$$

Since CP violation means that  $\mathcal{P}(\nu_\alpha \rightarrow \nu_{\beta \neq \alpha}) \neq \mathcal{P}(\bar{\nu}_\alpha \rightarrow \bar{\nu}_{\beta \neq \alpha})$ , CP violating terms must be an odd function of  $\delta_{\text{CP}}$ . Consider the following examples, muon neutrino survival and muon neutrino to electron neutrino appearance.

---

**1.1.2.2.1 Muon Neutrino Survival** The probability of a muon type neutrinos surviving is given by

$$\begin{aligned}\mathcal{P} \left( \langle \bar{\nu}_\mu \rangle \rightarrow \langle \bar{\nu}_\mu \rangle \right) = & 1 - 4s_{23}^2 c_{13}^2 \left( V_{\cos \delta_{\text{CP}}} \right) \sin^2 \phi_{31} \\ & - 4s_{23}^2 c_{13}^2 \left( Z_{\cos \delta_{\text{CP}}} \right) \sin^2 \phi_{32} \\ & - 4 \left( V_{\cos \delta_{\text{CP}}} \right) \left( Z_{\cos \delta_{\text{CP}}} \right) \sin^2 \phi_{21}\end{aligned}\quad (1.41)$$

where

$$V_{\cos \delta_{\text{CP}}} = s_{12}^2 c_{23}^2 + s_{13}^2 s_{23}^2 c_{12}^2 + 2s_{12}s_{13}s_{23}c_{12}c_{23} \cos \delta_{\text{CP}} \quad (1.42)$$

$$Z_{\cos \delta_{\text{CP}}} = c_{12}^2 c_{23}^2 + s_{13}^2 s_{23}^2 s_{12}^2 - 2s_{12}s_{13}s_{23}c_{12}c_{23} \cos \delta_{\text{CP}} \quad (1.43)$$

and  $\langle -\nu_\mu \rangle$  represents either  $\nu_\mu$  or  $\bar{\nu}_\mu$ . If a definitive measurement of  $\mathcal{P}(\nu_\mu \rightarrow \nu_\mu) \neq \mathcal{P}(\bar{\nu}_\mu \rightarrow \bar{\nu}_\mu)$  in vacuum occurs, this implies that the combined C, P and time (CPT) symmetry is violated<sup>4</sup>.

**1.1.2.2.2 Electron Neutrino Appearance** The previous subsection briefly explored the muon disappearance probability, which is not tested as a channel for CP violation. Electron neutrino appearance, however, does provide insight into CP violation in the lepton sector. The appearance probability of electron neutrinos types from muon types is given by

$$\begin{aligned}\mathcal{P} \left( \langle \bar{\nu}_\mu \rangle \rightarrow \langle \bar{\nu}_e \rangle \right) = & 4c_{13}^2 s_{13}^2 s_{23}^2 \sin^2 \phi_{31} \\ & + 8 \left( X_{\cos \delta_{\text{CP}}} \right) \cos \phi_{23} \sin \phi_{31} \sin \phi_{21} \\ & - \underbrace{8 \left( Y_{\sin \delta_{\text{CP}}} \right)}_{\text{CP violating}} \sin \phi_{32} \sin \phi_{31} \sin \phi_{21} \\ & + 4 \left( Z_{\cos \delta_{\text{CP}}} \right) s_{12}^2 c_{13}^2 \sin^2 \phi_{21}\end{aligned}\quad (1.44)$$

where

$$X_{\cos \delta_{\text{CP}}} = c_{13}^2 s_{12} s_{13} s_{23} (c_{12} c_{23} \cos \delta_{\text{CP}} - s_{12} s_{13}) \quad (1.45)$$

---

<sup>4</sup>When going to through matter however, the oscillation probability is affected. This is explained more in Section 1.1.2.3.

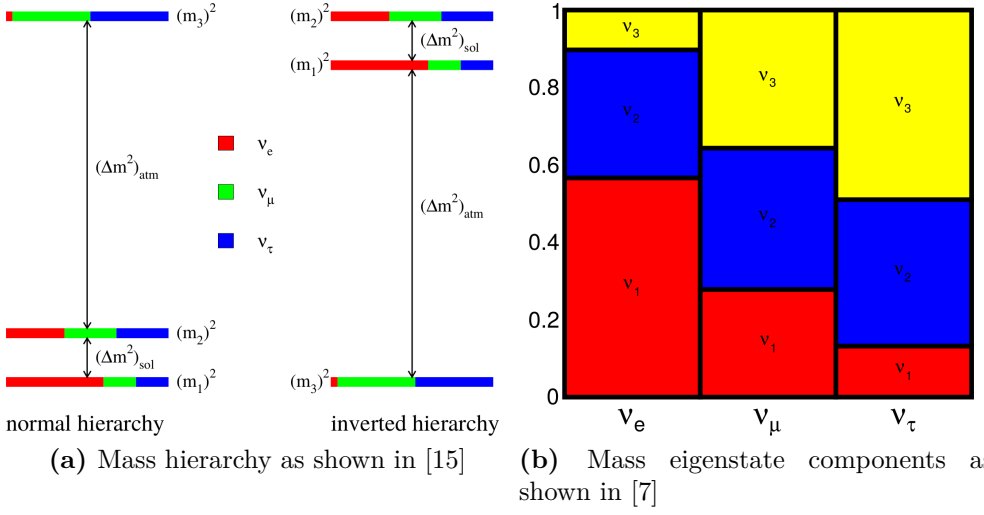


**Figure 1.8:** Left: the mass hierarchy problem is such that while the solar and atmospheric mixing mass-squared differences are clearly defined, the absolute mass scale is unknown. Since  $m_2 > m_1$  by definition, it is currently unknown if  $m_3$  is more or less massive than  $m_2$ , or even massless! Notice the colored bars for each mass eigenstate which corresponded to the approximate flavor content of the neutrino. For example, state “2” has about equal three portions of all three flavors. Right: the mass eigenstate components of each flavor eigenstate. This is a complementary demonstration of the MNSP matrix.

$$Y_{\sin \delta_{\text{CP}}} = \frac{1}{8} \sin(2\theta_{12}) \sin(2\theta_{13}) \sin(2\theta_{23}) c_{13} \sin \delta_{\text{CP}} \quad (1.46)$$

and (+) represents the sign change from neutrinos to anti-neutrinos. The CP violating term (1.46) is also known as the Jarlskog Invariant and is a measure of CP violation independent of the mixing parameterization [23]. This oscillation channel are of primary importance in current and future proposed accelerator and atmospheric neutrino oscillation experiments.

Current and next generation experiments aim to improve knowledge of the mixing parameters. There are a couple of degeneracies to unravel as well as precise measurement of  $\delta_{\text{CP}}$ . While the two defined mass-squared splittings  $\Delta m_{21}^2 = \Delta m_{\text{sol}}^2$  and  $\Delta m_{32}^2 = \Delta m_{\text{atm}}^2$  are known, it is unknown which eigenstates are more massive. This problem is known as the mass hierarchy problem and is illustrated in Figure 1.8a on page 22. Normal hierarchy refers to the case where  $m_3 > m_2 > m_1$  whereas the inverted hierarchy has  $m_2 > m_1 > m_3$ . Also knowledge if  $\theta_{23}$  is in the first octant  $\theta \in (0, \pi/2)$  or second octant  $\theta \in (\pi/2, \pi/4)$  requires large statistics. Finally the value of  $\delta_{\text{CP}}$  is quite uncertain with values in the 3rd and 4th

Parameter	Normal Hierarchy value	Inverted Hierarchy value	Units
$\Delta m_{32}^2 = \Delta m_{\text{atm}}^2$	$2.51 \pm 0.05$	$-2.56 \pm 0.04$	$10^{-3}$ eV $^2$
$\Delta m_{21}^2 = \Delta m_{\text{sol}}^2$		$7.53 \pm 0.18$	$10^{-5}$ eV $^2$
$\sin^2(\theta_{21}) = \sin^2(\theta_{\text{sol}})$		$0.307^{+0.013}_{-0.012}$	1
$\sin^2(\theta_{32}) = \sin^2(\theta_{\text{atm}})$	O1: $0.417^{+0.025}_{-0.028}$ O2: $0.597^{+0.024}_{-0.030}$	O1: $0.421^{+0.033}_{-0.025}$ O2: $0.592^{+0.023}_{-0.030}$	1
$\sin^2(\theta_{31})$		$2.12 \pm 0.08$	$10^{-2}$
$\delta_{\text{CP}}$	$217^{+40}_{-28}$	$280^{+25}_{-28}$	degrees

**Table 1.2:** Table of best fit MNSP parameters split by normal and inverted hierarchy. O1 and O2 correspond to the first octant ( $\theta \in (0, \pi/2)$ ) or second octant ( $\theta \in (\pi/2, \pi/4)$ ). All values except for  $\delta_{\text{CP}}$  are combined values from the Particle Data Group and  $\delta_{\text{CP}}$  is from the 2018 NuFit analysis [16, 34].

quadrants. Best fit measurements of the oscillations parameters is given in Table 1.2 on page 23.

### 1.1.2.3 Matter Effects

Traveling through matter has the potential to increase the sensitivity of oscillation measurements if the baseline is long enough. Known as the Mikheyev-Smirnov-Wolfenstein (MSW) effect [36], all oscillations are affected by coherent forward scattering of neutrinos with electrons in the media. Taking the example of  $\langle \bar{\nu}_\mu \rightarrow \bar{\nu}_e \rangle$  from (1.41), the MSW effect to first order is

$$\begin{aligned} \mathcal{P}(\langle \bar{\nu}_\mu \rightarrow \bar{\nu}_e \rangle) \rightarrow & \mathcal{P}(\langle \bar{\nu}_\mu \rightarrow \bar{\nu}_e \rangle) + \frac{8\alpha}{\Delta m_{31}^2} (c_{13}^2 s_{13}^2 s_{23}^2) (1 - 2s_{13}^2) \\ & \times \left( \sin^2 \phi_{31} \stackrel{(+)}{-} \underbrace{\left( \frac{\Delta m_{31}^2 c^3}{4\hbar} \frac{L}{E_\nu} \right)}_{\phi_{31}} \cos \phi_{32} \sin \phi_{31} \right), \end{aligned} \quad (1.47)$$

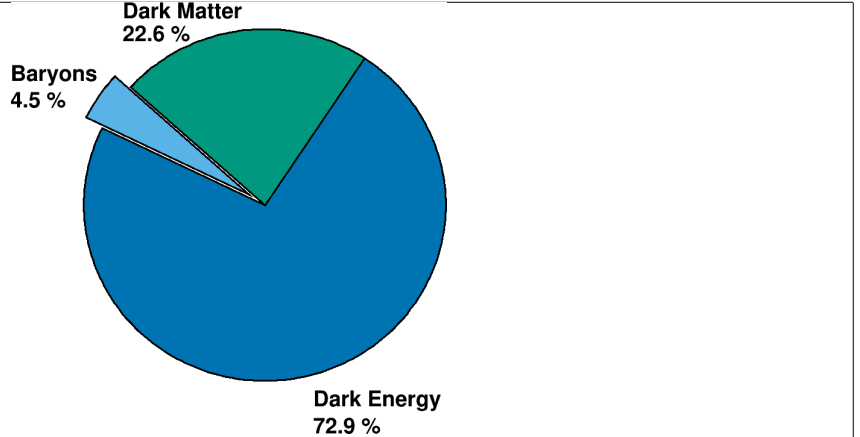


**Figure 1.9:** Display of the matter and energy content of the Universe. The observed content is 4.5% of baryonic matter. The rest of the Universe consists of non-baryonic matter called Dark Matter and a form of energy called Dark Energy. These inferred parameters are taken from the  $\Lambda$ CDM model, the simplest model that describes the cosmos [24].

where

$$\alpha = 2\sqrt{2}G_F n_e E_\nu \quad (1.48)$$

and  $G_F$  is the Fermi constant and  $n_e$  is the average electron density of the Earth which the neutrinos travel [8]. Carefully studying (1.47) reveals that the MSW effect alters the oscillation probability as a function of the electron density and increases in magnitude with baseline.

### 1.1.3 CP Violation: Origins of Matter

To conclude the introduction on neutrinos, it is important to examine the implications of CP violation. The observation of CP violation in the lepton sector might provide critical insight into the origins of the matter. CP violation dictates that certain interactions behave differently between matter or antimatter like  $\mathcal{P}(\nu_\mu \rightarrow \nu_e) \neq \mathcal{P}(\bar{\nu}_\mu \rightarrow \bar{\nu}_e)$ . The Big Bang Theory suggests that in the first fractions of a second of the Universe, equal amounts of matter and antimatter were created. However, observational evidence shows the Universe consists of only 4.5% baryonic matter (i.e. protons and neutrons) from cosmological models as shown in Figure 1.9 on page 24. The anti-baryonic fraction of the baryonic matter is

---

infinitesimally low from external constraints on data from gamma-ray telescopes like Fermi-GLAST [35]. This problem is known as the Baryon Asymmetry of the Universe (BAU).

The process of Baryogenesis<sup>5</sup> is a favored model to explain the BAU and lacks a necessary precursor mechanism. One of the necessary conditions for Baryogenesis [30] is C symmetry violation and CP violation. Evidence of CP violation has been experimentally confirmed in the quarks, but not to the level which resolves the BAU. Baryogenesis can be achieved by having Leptogenesis<sup>6</sup> occur first through the decay of very heavy, right handed Majorana neutrino ( $\nu = \bar{\nu}$ ) through the *see-saw* mechanism. Detailed discussions on Leptogenesis and the *see-saw* mechanism can found in [7].

## 1.2 Tokai-to-Kamioka Experiment

The Tokai-to-Kamioka (T2K) experiment is a long baseline, neutrino oscillation experiment hosted in Japan [1] as shown in Figure 1.10 on page 26. It is the successor experiment to the KEK-to-Kamioka neutrino oscillation experiment also hosted in Japan. T2K produces its high intensity, muon neutrino pure beam at the Japan Proton Accelerator Complex (J-PARC), a world class particle accelerator facility. The beam is directed at the Super-Kamiokande (SK) [19] detector which is 295 km away from the source. Along the beamline at 280m from the beam source are a series of near detectors called ND280 [17] to observe and characterize the unoscillated beam. This thesis uses data from ND280 detector to test for increased sensitivity to beam characterization. The beam is designed to maximize the  $\nu_\mu \rightarrow \nu_e$  probability at the  $L = 295$  km baseline using a neutrino energy spectrum sharply peaked at  $E_\nu = 0.6$  GeV as shown in Figure 1.11 on page 26. This spectrum is achieved by directing the center of the beam axis 2.5 degrees off center from SK.

---

<sup>5</sup>Baryogenesis is the mechanism by which matter and antimatter baryons are created in the early Universe.

<sup>6</sup>Leptogenesis is the mechanism by which leptons and anti-leptons are created in the early Universe.

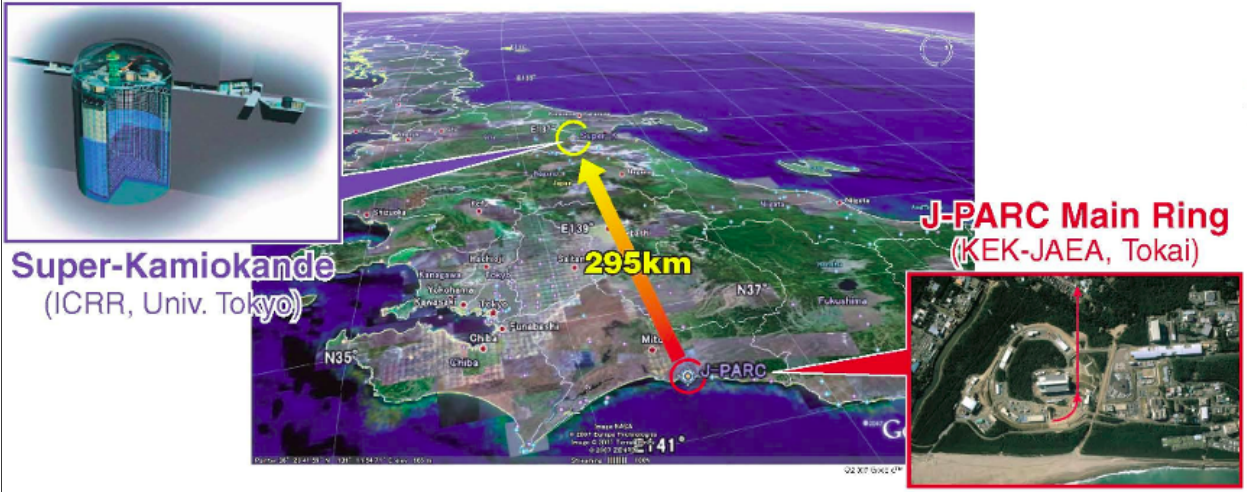


**Figure 1.10:** Birds eye view of the T2K experiment on the Japanese archipelago. An intense beam of neutrinos are produced at the J-PARC site (bottom right red box) using high energy protons. The beam is directed towards the Super-Kamiokande detector (top left blue box) at a distance of 295 km away from J-PARC.

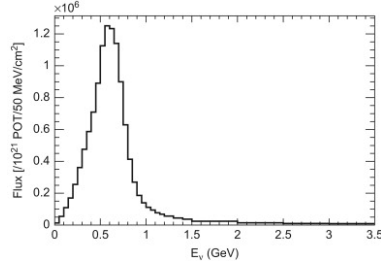


**Figure 1.11:** The T2K unoscillated  $\nu_\mu$  flux at SK at the off-axis angle of  $2.5^\circ$ .

T2K was primarily designed to measure the last unknown MNSP mixing angle  $\theta_{13}$ , which was thought to be nearly zero. In addition it set out to measure to high precision the atmospheric mixing parameters,  $\theta_{23}$  and  $\Delta m_{23}^2$ . One of its early successes was a landmark  $7.3\sigma$  measurement of a non-zero  $\theta_{13}$  using the electron-neutrino appearance measurement [3]. It continues to be a world leader in oscillation physics and as of 2018 rejects CP conserving values ( $\delta_{\text{CP}} = 0, \pi$ ) at the  $2\sigma$  level [5].

The following topics will be discussed in the following order. First a look how neutrinos are produced at J-PARC. Next a detailed look at the T2K near detectors which are used in this thesis. This is followed by a discussion on Super-Kamiokande, the T2K far detector.

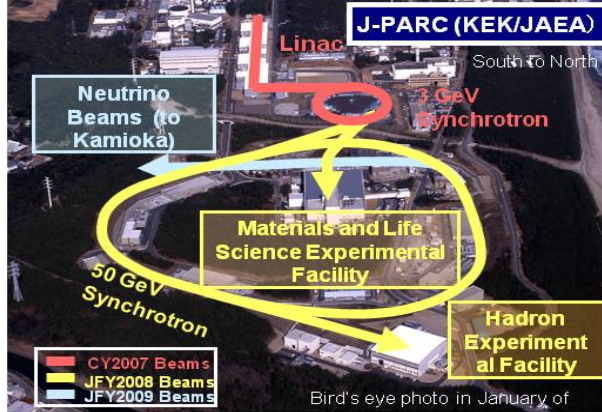


**Figure 1.12:** Bird's eye view of the J-PARC center showing the primary components of its accelerator programs. To generate the high intensity neutrino beam, first the linear accelerator (Linac, red) accelerates hydrogen ions (protons) into the 3 GeV Synchrotron (also red) called the rapid-cycle synchrotron (RCS). The RCS then injects some of its protons into the 50 GeV Synchrotron (yellow) called the main ring (MR) which currently runs at 30 GeV. Finally the MR protons are directed into a target material along the neutrino beamline (teal) [11].

### 1.2.1 Neutrino Production at J-PARC

To facilitate the high intensity neutrino beam requirements for T2K, the J-PARC site generates a high intensity proton beam through a series of particle accelerators. A bird's eye view of J-PARC can be seen in Figure 1.12 on page 27 which highlights its different accelerators and facilities. For this section, note that all beam energies are kinetic energies.

Protons for the T2K beamline are first accelerated in the J-PARC linear accelerator<sup>7</sup> (linac) and then the rapid cycle synchrotron<sup>8</sup> (RCS). Hydrogen ions ( ${}^1\text{H}^-$ ) are extracted from plasma in a electrical discharge chamber and feed through a series of linac elements as shown in Figure 1.13a on page 28. Each linac element except for the initial quadrupole magnet apparatus accelerates the ions using carefully coordinated oscillating electric fields generated by radio frequency pulses. After traveling 240m along the linac, the ions have been

<sup>7</sup>A linear accelerator accelerates particles using time varying electric fields along a one direction, terminal beamline. Not only used in particle physics, they are also used in the medical field to generate X-rays.

<sup>8</sup>A synchrotron is cyclic particle accelerator that relies on time varying magnetic fields to accelerate particles. Since they require many magnets and large spaces to operate, they are usually operated at national laboratories for others uses as well like material and life sciences.

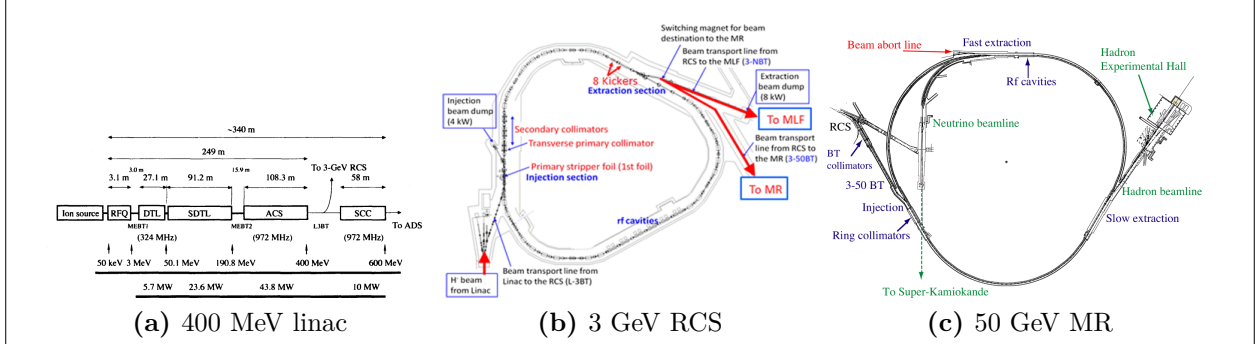


**Figure 1.13:** Schematics of the J-PARC accelerators. (a) The linac accelerates hydrogen ions to 181 MeV of kinetic energy, designed for 400 MeV, from the ion source through linear accelerator (linac) elements [37]. (b) Protons from the linac are collected into the rapid cycle synchrotron (RCS) and accelerated to 3 GeV [29]. (c) Protons from the RCS are injected into the main ring (MR) synchrotron which further accelerates the protons. While the MR is designed for 50 GeV, it currently operates at 30 GeV. For T2K, the protons are bunched in the MR and extracted into the “Neutrino beamline” [22].

boosted to 181 MeV of kinetic energy and transported into the RCS. In transit to the RCS, the ions are stripped of their electrons via charge stripping foils. The 348m circumference RCS then further boosts the protons to 3 GeV at an operating frequency of 25 Hz. While being accelerated, protons are aggregated into two bunches and focused using particle collimators as shown in Figure 1.13b on page 28.

The next stage for the protons intended for the neutrino beamline is the much larger main ring (MR) synchrotron as shown in Figure 1.13c on page 28 which has a circumference of 1567m. While nominally designed to boost protons to 50 GeV, it currently operates at 30 GeV. Protons are injected into the MR to form eight proton bunches (spill), initially six when T2K first ran, before entering the neutrino beamline. The total temporal width of the spill is approximately  $0.5\mu\text{s}$  [1]. At a spill cycle frequency of 0.5Hz, the bunches are extracted from the MR into the neutrino beamline.

The neutrino beamline is designed to direct the protons toward SK and generate neutrinos by striking them on a cylindrical target. Figure 1.14a on page 29 shows the process of proton extraction from the MR for both primary and secondary neutrino beamlines. In the primary beamline, a series of normal and superconducting magnets steer the proton beam away from

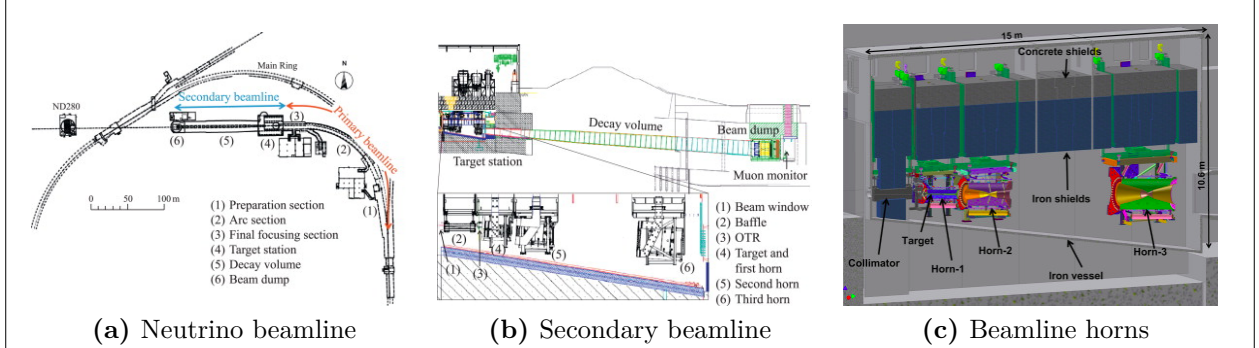
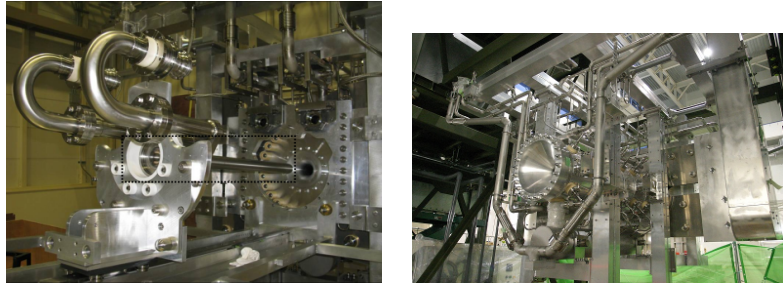


**Figure 1.14:** The neutrino beamline at J-PARC consists of a primary and secondary beamline. (a) The primary beamline redirects the protons towards the secondary beamline [1]. (b) In the secondary beamline, the protons are impinged on a cylindrical target producing mostly pions. The pions are focused using in sequence horns and decay in a long decay volume. Any non-decayed particles are stopped at the beam dump. (c) A further zoomed in cross section of the target station showing the target and focusing horns [33].



(a) A graphite target being extracted from the target station (b) A magnetic focusing horn

**Figure 1.15:** Shown are photos of work performed on the target station. (a) The graphite rod being extracted from the target station is shown in the black-dashed box. (b) One focusing horn in T2K.

the MR first along a 54m preparation section and then a 147m arc section to bend the beam towards SK. A final focusing section in the primary beamline focuses the protons into the secondary beam while directing it downwards  $3.637^\circ$  with respect to the local horizontal. Since a well tuned and stable proton beam is necessary for neutrino production, numerous beam monitors are installed along the primary beamline to measure any losses.

The secondary beamline marks the end of the proton beam and production of a neutrino beam. In the secondary beamline, as shown in Figure 1.14b on page 29, it consists of a target station, a decay volume for the outgoing particles from the target station, and a beam dump for any remaining particles. The target station houses a 91.4cm long, 2.6cm

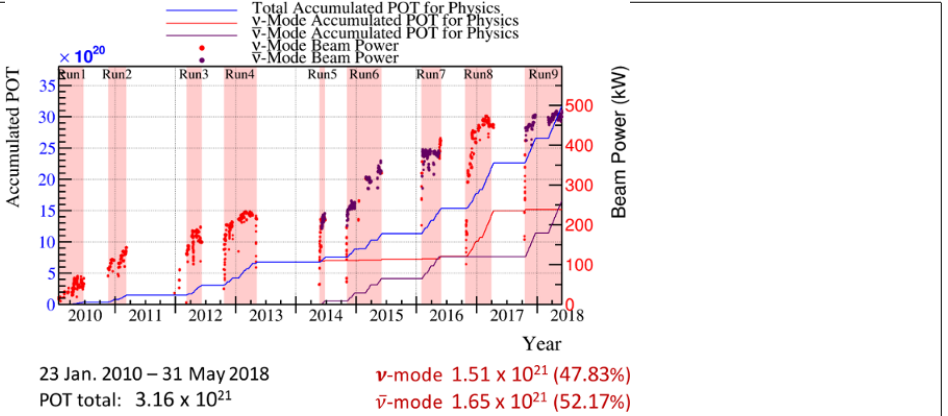


**Figure 1.16:** T2K accumulated protons on target since 2010 shows a steady increase in beam power over time. The gap between Run2 and Run3 is due to the damage suffered at J-PARC after the 2011 Tōhoku earthquake.

diameter, and  $1.8\text{g}/\text{cm}^3$  graphite rod which corresponds to 1.9 radiation lengths. When the protons strike the target, strong (nuclear) interactions produce  $\pi(\pi)$ -mesons (pions) and K-mesons (kaons). like those produced from cosmic ray collisions in the upper atmosphere. To enhance the flux of neutrinos, a series of three current pulsed, focusing magnets called horns<sup>9</sup> as shown in Figure 1.14c on page 29 are used to focus the mesons of the correct charge towards SK. Photographs of a graphite target and focusing horn are shown in Figure 1.15 on page 29. The horns are pulsed at +250kA (-250kA) to select positively (negatively) charged pions. The focused pions are allowed to decay along the 96m long decay volume as to boost the daughter neutrinos along the secondary beamline direction. For safety reasons, the decay volume is filled with gaseous helium at 1 atm of pressure which has a low pion absorption rate. The daughter particles in the decay volume should be mostly muons and muon-neutrinos traveling towards SK. A beam dump is placed at the end of the decay volume to stop particles that have not yet decayed to prevent uncontrolled decay products from contaminating the beam.

Along both beamlines are numerous monitors and timing systems to observe the proton beam to ensure stable production of neutrinos. Proton beam monitors are placed along the

<sup>9</sup>The name horn derives from the fact that the focusing magnets are shaped like brass horns in a music ensemble or marching band. One can think of these horns like a focusing lens for charged particles.

---

primary beamline to ensure the proton beam is properly steered into the secondary beamline. An optical transition radiation monitor is situated around the target to observe any protons not intersecting with the target region itself. The last monitor along the secondary beamline is the a muon monitor (MUMON), which is placed downstream of the beam dump to observe the daughter muons of  $> 5$  GeV/c momentum [1].

In order to provide timing information for the neutrino beam at SK, a global positioning system (GPS) is used to synchronize clocks at SK and J-PARC. Any event outside the beam timing window are rejected in the T2K oscillation analysis, and so having precise timing information for the neutrino beam is critical for the experiment. The GPS has an internal accuracy of 50ns, or about  $\sim 150$ m assuming the neutrinos are traveling near the speed of light. This is well within the time it takes for any neutrino to travel the 295 km between J-PARC and SK.

J-PARC continues to improve the proton delivery and neutrino modes since T2K began in 2010. T2K has run in two horn current modes:  $\nu$ -mode and  $\bar{\nu}_\mu$ -mode. Focusing positively charged pions with +250 kA horn current is called forward horn current (FHC) mode. Similarly, using -250 kA horn current is called reverse horn current (RHC) mode. The aggregate running of T2K for both FHC and RHC modes are shown in Figure 1.16 on page 30 in units of protons on target (POT).

In addition the proton beam intensity, as measured in kW (energy/proton/second), has been increased over time which increases the number of neutrino interactions observed at SK. Note that while  $\pm 250$  kA is the preferred horn current in both FHC and RHC modes, the horns were run briefly at +205kA when operations resumed after 2011 Tōhoku earthquake.

### 1.2.2 Neutrino Near Detectors: ND280

T2K has a near detector (ND) site at J-PARC that is designed specifically observe the neutrinos in flight aimed at Super-K. The purpose of a ND site is to *constrain the neutrino flux and interaction rate* at SK in order to reduce the impact of their systematic uncertainties

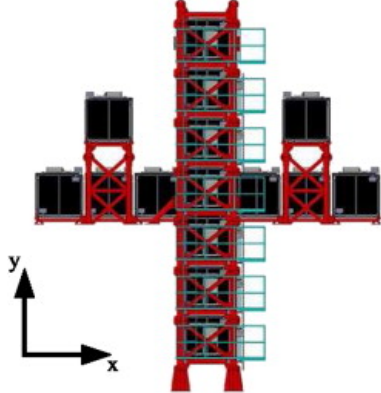


**Figure 1.17:** A schematic of INGRID shows the arrangement of the tracking scintillating modules. There are 16 identical modules total with seven in the vertical row, seven in the horizontal row, and two at off-axis positions. INGRID is capable of measuring the neutrino beam in a transverse area of  $10\text{m} \times 10\text{ m}$ . With the vertical row upstream of the horizontal row, the designed beam center intersects each row's center module [2].

in the oscillation analysis. The analysis in this thesis uses the data provided by the off-axis ND. The site is called ND280 and is located 280m away from the production target. The primary detector is an off-axis, magnetized tracking detector consisting of different subdetectors. A separate detector array called the Interactive Neutrino Grid (INGRID) measures the neutrino beam profile. Both on-axis and off-axis detectors extensively utilize a commercial light sensor called a multi-pixel photon counter (MPPC) for the light collection in the scintillator-based detectors.

The following subsections begin with a description of the MPPC technology used in T2K. Next is a description of INGRID and its purpose at ND280. This is followed by a general description primary off-axis, magnetized detector. The last two subsections are descriptions of two primary subdetectors in the off axis detector. The first and second being the pi-zero detector (PØD) and time projection chamber (TPC), respectively.

From here on unless specified, INGRID will refer only to the on-axis ND and ND280 will refer only to off-axis ND.

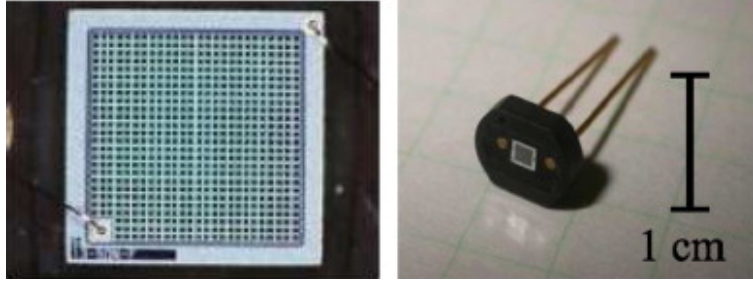


**Figure 1.18:** Photographs of the specially designed MPPC used in T2K. A magnified face view is shown on the left with an entire unit shown on the right [1].

### 1.2.2.1 Multi-pixel photon counter (MPPC)

While the reliable photo-multiplier tube (PMT) technology was used in previous scintillator-based detectors, T2K needed a different technology to work in the strong magnetic field environment. T2K selected a commercially available silicon photomultiplier sensor developed by the Hamamatsu corporation called a MPPC. A MPPC is a compact device containing many sensitive avalanche photodiode pixels that act as Geiger micro-counters. They are well matched with the spectral emission of wavelength-shifting (WLS) fibers used to collect the scintillator light in ND280 and operate in a strong magnetic field environment. T2K utilizes specialized 667-pixel MPPCs with an effective area of  $1.3\text{ mm} \times 1.3\text{ mm}$  as shown in Figure 1.18 on page 33.

### 1.2.2.2 On-Axis Detector

The on-axis near detector called the Interactive Neutrino Grid (INGRID) is a tracking scintillator detector designed to directly measure the neutrino beam profile. As shown in Figure 1.17 on page 32, it is a cross grid of tracking modules centered at the designed neutrino beam center ( $\theta = 0$ ). Each module consists of alternating layers of iron plates and scintillator bars except for the two most downstream scintillating layers which lack iron plates. To monitor any beam asymmetry, two separate modules are placed off the grid axis.

Each scintillating bar consists of scintillator-doped polystyrene which emits light when a charged particle deposits energy in the media. Each bar contains a single wavelength-

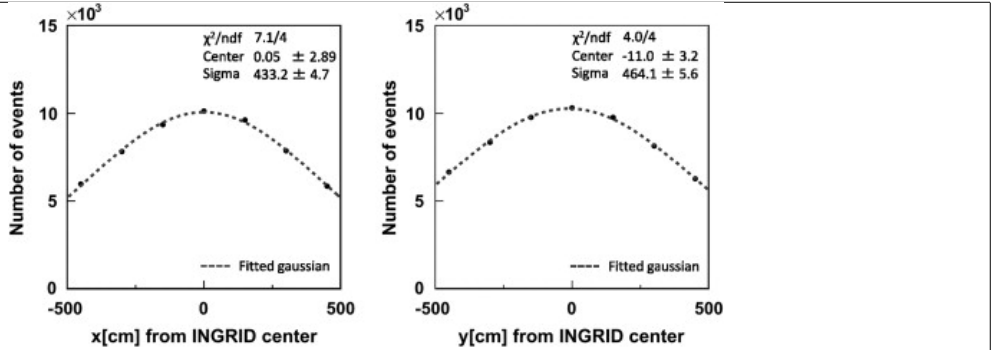


**Figure 1.19:** A beam profile taken with INGRID in April 2010 shows the Gaussian nature of the beam. The errors on the data points are about 1%. [2]

shifting (WLS) fiber to collect and shift the light to a different energy. The light is collected at a single MPPC device and converted into an electrical signal. In order to enhance the collection efficiency, a reflective  $\text{TiO}_2$  doped polystyrene shell surrounds each bar. Bars are assembled into planes to provide tracking capabilities. Veto planes also surround each module to prevent false signals to trigger.

INGRID is continuously operated to check that the neutrino beam center was properly aligned at its designed center. Diagnostic plots such as Figure 1.19 on page 34 are collected on a monthly basis to ensure that the neutrino flux at Super-Kamiokande (SK) is consistent with T2K's design. A history of the beam profile and event rate on INGRID between January 2010 and October 2016 is shown in Figure 1.20 on page 35.

### 1.2.2.3 Off-Axis Detector Summary

The near detector in T2K is ND280, which is an off-axis, magnetized tracking detector. It is a collection of different detector technologies designed to facilitate three primary measurements:

1.  $\nu_\mu$  flux at SK,
2. Irreducible  $\nu_e$  background flux at SK, and
3.  $\nu_\mu$  interaction backgrounds and cross sections for the  $\nu_\mu \rightarrow \nu_e$  search.

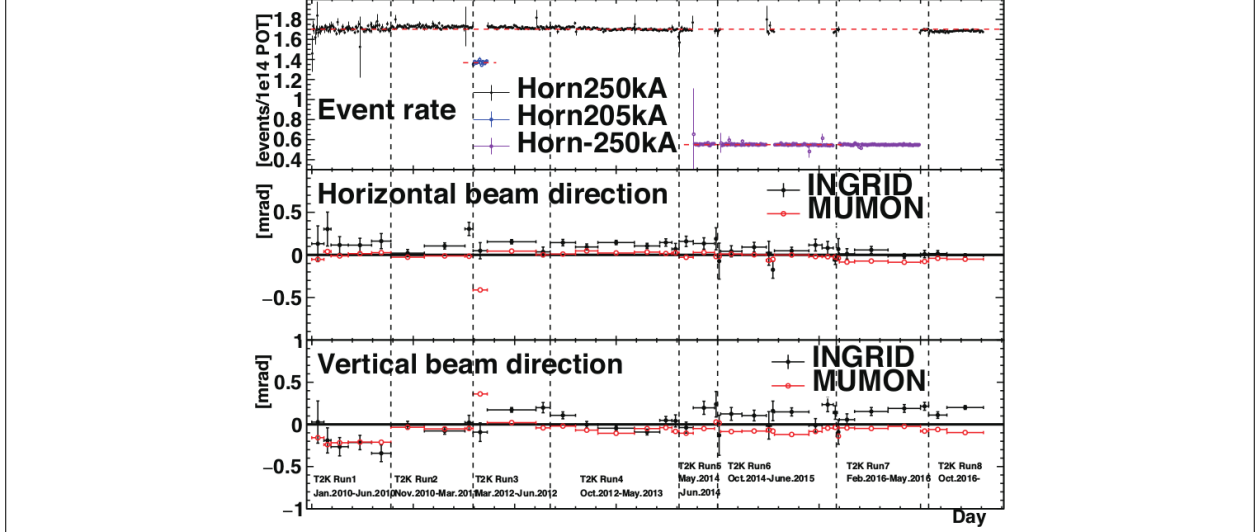


**Figure 1.20:** INGRID interaction event rate and beam profiles are shown. The top panel shows the event rate for the three different horn currents. The middle and bottom panels show the horizontal and vertical beam directions with respect to the beam center, respectively. A deviation of 1 mrad corresponds to a little under 30 cm. The error bars shown are the statistical errors on the mean.

ND280 consists of the pi-zero detector (PØD), the tracker region consisting of a fine grain detector (FGD) and time projection chamber (TPC), an electromagnetic calorimeter (ECal), and side muon range detector (SMRD). The ND280 subdetectors are instrumented inside the recycled UA1/NOMAD magnet with the SMRD in the magnetic field return yoke itself. All but the FGD is instrumented with the same scintillating-bar bar technology collected by MPPCs. A schematic of the different detector components of ND280 is shown in Figure 1.21 on page 36.

The analysis in this thesis use measurements from the primary subdetectors, the PØD and the TPC. The PØD serves as a massive target for the incident neutrino beam and the TPC serves to measure the charge and momentum of the outgoing particles.

The ND280 magnetic field is generated using electrical current fed through solenoid coils to generate a dipole field of strength  $0.2\text{ T}^{10}$  in the x direction. The field is highly uniform

<sup>10</sup>This is a powerful magnetic field. According to the The US/UK World Magnetic Model for 2015-2020, the magnetic field strength on the surface of the Earth is about 0.294385 Gauss or  $2.94385 \times 10^{-5}\text{ T}$ . So the field inside ND280 is about 6800 times more forceful than the Earth's influence [12].

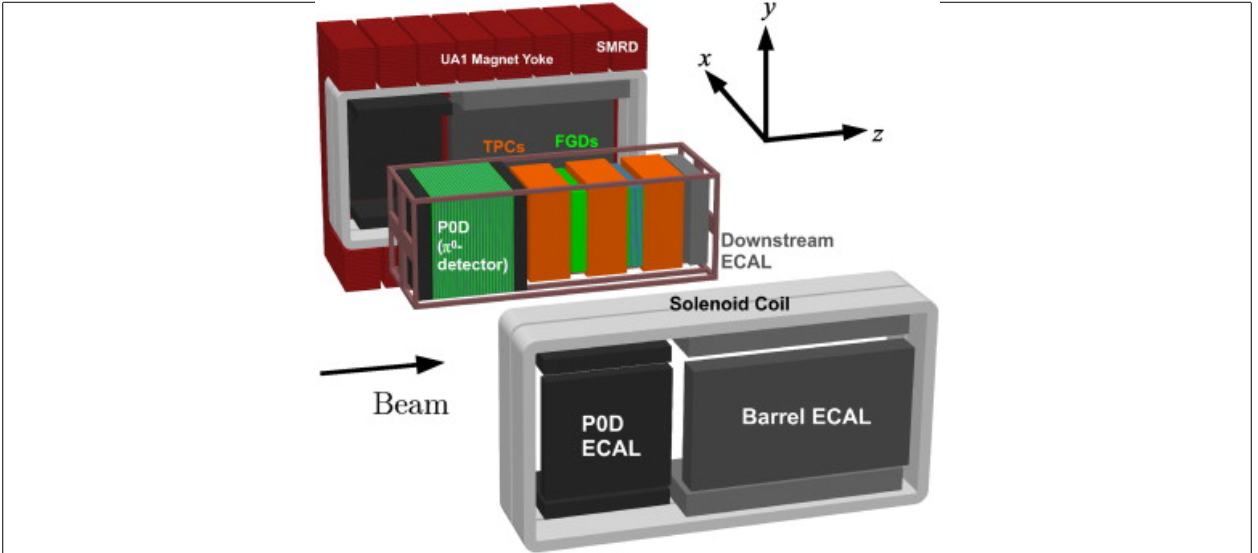


**Figure 1.21:** An exploded view of the ND280 off-axis detector. The magnetic field is generated from the Solenoid Coil via an electrical current which produces a dipole magnetic field of strength 0.2 T. The field is designed to return to the Magnetic Yoke.

near the center of the detector which is where the majority of the TPC system is located. However, it has significant deviations from 0.2 T near the solenoid edges. In order to fully understand the field inside ND280, a precise 3D model was generated using a machine controlled Hall probe. The operating field strength during the mapping process was 0.07 T due to power restrictions at the time. The model was then compared with measurements in the TPC region as shown in Figure 1.22 on page 37. After scaling the model to the nominal operating strength of 0.2 T, a fractional uncertainty of  $10^{-3}$  or uncertainty of 2 Gauss in each direction was obtained.

The ND280 magnetic field permits the measurements of particle charge and momentum. A particle of charge  $q$ , rest mass  $m_0$ , and velocity  $\mathbf{v}$  under the influence of an external electric and magnetic fields,  $\mathbf{E}$  and  $\mathbf{B}$ , respectively, experiences a force  $\mathbf{F}$  given by the Lorentz force equation

$$\mathbf{F} = q(\mathbf{E} + \mathbf{v} \times \mathbf{B}). \quad (1.49)$$

Assuming for now that there is no external electric field, the force on the particle is

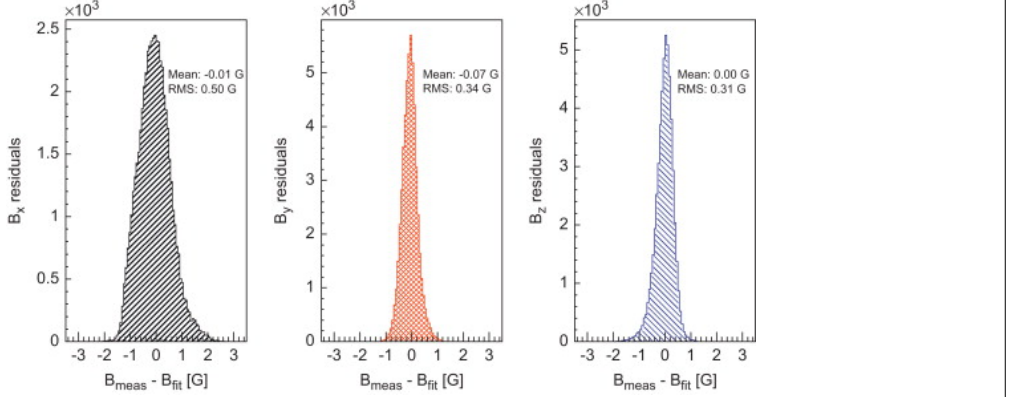


**Figure 1.22:** Each of the magnetic field components (x, y and z, respectively) are compared between a fit of the data and the actual measurements near the center of ND280. The systematic uncertainty on the field is extracted from the RMS of the mapping [1].

$$\mathbf{F} = q\mathbf{v} \times \mathbf{B}, \quad (1.50)$$

which is both orthogonal to  $\mathbf{v}$  and  $\mathbf{B}$ . Since the mechanical work on a particle in a magnetic field is zero, the particle's energy is unchanged ( $|\mathbf{v}| = v = \text{constant}$ ). Newton's Second Law allows us to rewrite the force as an change in momentum  $\mathbf{P}$

$$\begin{aligned} \mathbf{F} &= \frac{d\mathbf{P}}{dt} \\ &= \frac{d}{dt} (\gamma(v)m_0\mathbf{v}) \\ &= m_0\mathbf{v} \left( \frac{d\gamma(v)}{dt} \right) + \gamma(v)m_0 \left( \frac{d\mathbf{v}}{dt} \right) \\ &= m_0\mathbf{v} \left( \frac{d\gamma(v)}{dv} \right) \cancel{\left( \frac{dv}{dt} \right)}^0 + \gamma(v)m_0\mathbf{a} \\ &= \gamma(v)m_0\mathbf{a}, \end{aligned} \quad (1.51)$$

where  $\mathbf{P} = \gamma(v)m_0\mathbf{v}$  is the relativistic momentum and  $\gamma(v) = (1 - (v/c)^2)^{-1/2}$  is the Lorentz factor for relativistic particles. For uniform circular motion, the magnitude of the acceleration is given by

$$|\mathbf{a}| = v^2/R, \quad (1.52)$$

where  $R$  is the radius of curvature for the circle. Combining equation (??) and equation (??) with some algebra yields

$$R = \frac{\gamma(v)m_0v}{q|\mathbf{B}|\sin\theta_{\mathbf{vB}}}, \quad (1.53)$$

where  $\theta_{\mathbf{vB}}$  is the angle between  $\mathbf{v}$  and  $\mathbf{B}$ . The numerator of equation (??) is recognized as the magnitude of the momentum  $|\mathbf{P}|$ . Some further rearrangement yields

$$|\mathbf{P}| = q|\mathbf{B}|R\sin\theta_{\mathbf{vB}}, \quad (1.54)$$

and thus measuring the direction and radius of curvature inside the field provides the charge and momentum, respectively, as desired.

#### 1.2.2.4 Off Axis pi-zero detector (PØD)

The PØD is the primary detector used a neutrino target in this thesis. It is a plastic scintillator based tracking calorimeter inside the ND280 magnet region. It is designed to measure the neutral current (NC) process  $\nu_\mu + N \rightarrow \nu_\mu + N + \pi^0 + X$  on water where  $N$  is a nucleus and  $X$  is any set of final state particles. NC  $\pi^0$  was expected to be a significant background in the  $\nu_e$  appearance search in the likelihood that  $\theta_{13} \approx 0$ . The PØD is a modifiable detector which can be filled or drained of water during data taking, enabling the determination of water target (WT) cross sections by comparing water-in data with water-out data.

A representation of the PØD is shown in Figure 1.23 on page 39. The active detector components are very similar to INGRID's design where scintillation light is captured by a WSF and counted by a MPPC. Each bar is triangular in shape as shown in Figure 1.24 on page 40. A plane of 134 horizontal and 129 vertical bar together to form a PØD module (PØDule) as shown in 1.23b. The PØD dimensions are  $2.298 \times 2.468 \times 2.350\text{m}^3$ , in XYZ respectively, with a total mass of  $\sim 1900$  kg of water and 3570 kg of other material. The total mass of the PØD is approximately 15,800 kg when the bags are full of water. PØDules are

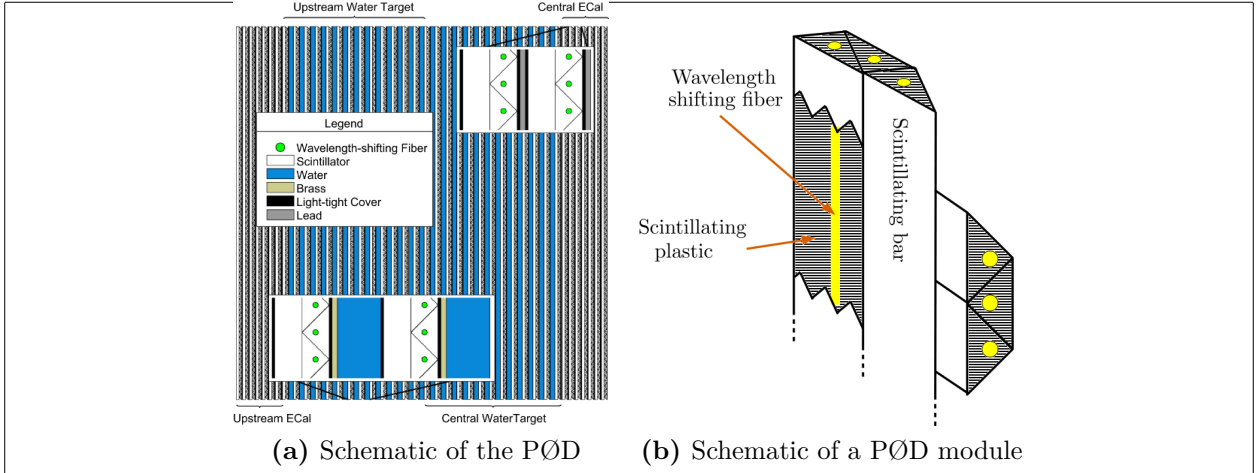


**Figure 1.23:** Schematics of the PØD. Left: insets detail the Water Target and ECal layers. Right: A view of a PØD module illustrating the orthogonal layout of the scintillating planes. Both: the neutrino beam is coming from the left.

Element	Symbol	Fraction [%]
Carbon	C	45.0
Oxygen	O	29.9
Copper	Cu	14.3
Hydrogen	H	8.0
Zinc	Zn	1.6
Chlorine	Cl	1.1
Titanium	Ti	0.1

**Table 1.3:** Elemental composition of PØD water target region. The table is sorted from top to bottom by fraction of mass. This table was originally produced in Reference [6]

arranged into three primary regions. The water target (WT) region contains 26 PØDules interleaved between bags of water 2.8 cm thick when filled and 1.3 mm thick brass sheets designed to help contain  $\pi^0$  decay photons. The last two regions are the upstream ECal (USECal) central ECal (CECal). Each ECal region contains 7 PØDules with steel sheets clad with lead between them [6]. An elemental composition of the WT is shown in Table 1.3 on page 39.

The readout electronics for the PØD is based on the Trip-T application specific integrated circuit (ASIC) shared among the SMRD, ECals, and INGRID. Signals from 64 MPPCs are

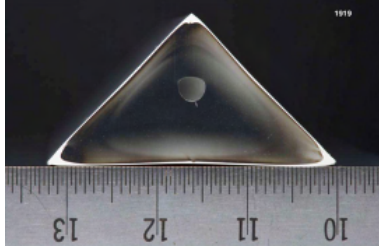


**Figure 1.24:** A cross section of a PØD scintillating bar. The base and height is 33 mm long and 17 mm high. The wavelength shifting fiber is inserted in the bored hole which is half-way between the base and tip.

routed to Trip-T front end boards (TFB) that each house 4 Trip-T ASICs. Each Trip-T collects the MPPC charge in 23 programmable integration cycles.

The TFB are readout to back-end electronics which control the TFBs and synchronize clocks. A total of six readout merger module (RMM) electronics receive TFB the data and control each TFB ASIC. RMM timing are synchronized with a cosmic trigger module and a slave clock module (SCM), of which both are synchronized with a master clock module from the beamline. Synchronizing the RMMs with the SCM allows for the Trip-T ASIC integration windows to match with the beam. The RMMs are responsible for distributing the TFB data to the data acquisition (DAQ) system for storage.

The ND280 DAQ consists of a MIDAS framework to monitor and control data collection. The primary client of the DAQ is to merge data and package it for long term storage. In parallel to it is the Global Slow Control (GSC) system which measures temperatures, voltages, and other physical quantities. Together the DAQ and GSC help scientists consistently produce high quality data and maintain the overall stability of the detector.

### 1.2.2.5 Off Axis Time Projection Chamber (TPC)

The ND280 TPC is designed to provide momenta measurements of charged particle tracks as discussed above, high resolution particle counting capabilities, and particle identification based on energy deposition. The latter most aspect is not utilized in this thesis. The TPC is divided into three volumes separated by the two FGD volumes. Each TPC volume

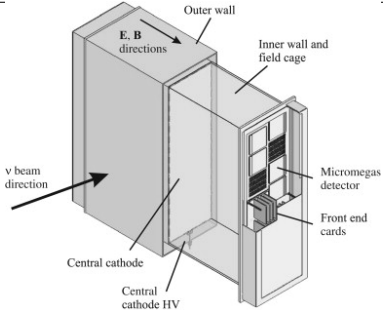


**Figure 1.25:** Cut-away drawing of a TPC volume in ND280 [1].

( $2.3 \times 2.4 \times 1.0 \text{ m}^3$ ) consists of an inner box that holds an argon-based gas and an outer box that holds an insulating CO<sub>2</sub> gas. The inner gas mixture is 3000 L of Ar:CF<sub>4</sub>:iC<sub>4</sub>H<sub>10</sub> (95:3:2) gas. It was selected for its high speed, low diffusion, and good performance with the micromegas [1]. A simplified schematic of the TPC is shown in Figure 1.25 on page 41.

As charged particles traverse the inner TPC volume, they create ionization electrons in the gas which drift towards readout planes away from a central cathode. The electron drift acceleration is rapid due to the strong 5 kV/cm electric field present. Drift electrons are multiplied and sampled by micromega detectors that line the sides of the TPC, providing nearly 3 m<sup>2</sup> of active surface coverage. Arrival times of the electrons provide timing information to give a full three dimensional portrait of the events.

#### 1.2.2.6 Track Reconstruction in ND280

The goal of track reconstruction software is to capture the shape and history of energy deposited in the detector. Since ND280 is collection of different technologies, highly specific algorithms and models are used to identify track-like patterns. Since this analysis uses neutrino events incident in the PØD and cross into the TPC, an unified and coherent reconstruction model. A reconstruction package called “Global” is designed to combine all ND280 information for this purpose.

For PØD tracks,

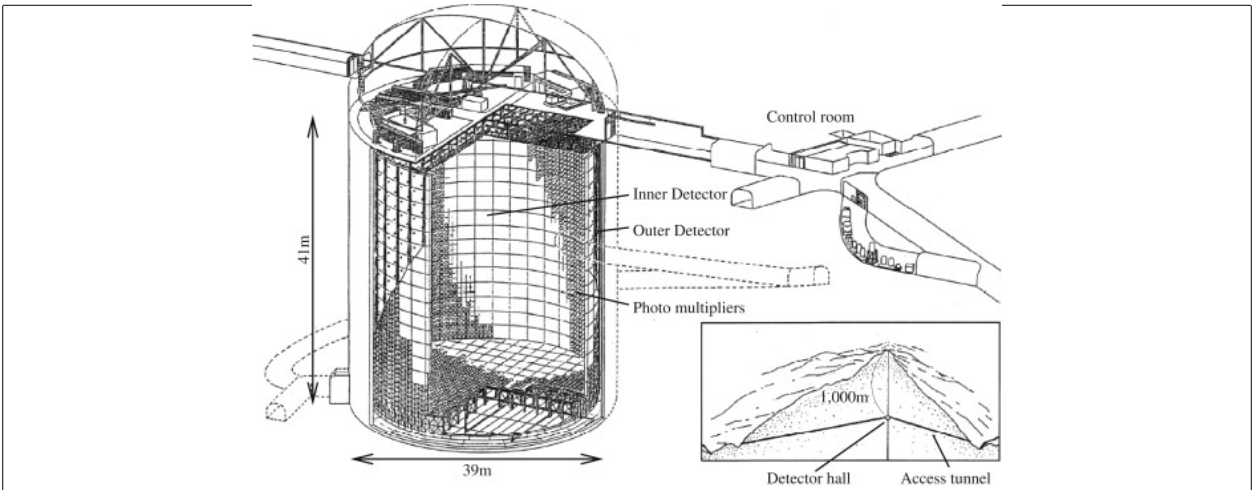


**Figure 1.26:** Diagram of the Super-Kamiokande detector consisting mainly of the inner and outer detector segments. The boundary between the two segments is cylindrical scaffolding used to mount photomultiplier tubes and optically isolate the segments.

### 1.2.3 Neutrino Far Detector: Super-Kamiokande

The Super-Kamioka neutrino detection experiment (Super-Kamiokande) is the dedicated far detector for the T2K experiment. Sitting at 295 km away from the neutrino source with a 1 km overburden, it is well designed to detect the elusive neutrino. Containing about 50 kt of pure water, is it lined with PMTs in both an inner and veto outer detector as shown in Figure 1.26 on page 42.

When charged particles travel through the water, a Cherenkov radiation cone is produced. The sharpness of the cone edge is an unique ID for the particle species that produced it. An electron produces a fuzzy edge since it experiences many large multiple scatterings off the water molecules. A muon on the other hand produces a sharp edge since it is much more massive and thus less perturbed by the water molecules. Both types of events are shown in Figure 1.27 on page 43. By determining the particle that produced it and isolating the event during the T2K beam, the neutrino flavor is deduced.

While events from SK are not used in this analysis, the goal is to try to improve T2K's parameters which depend on comparing the Near Detector neutrino measurements to the

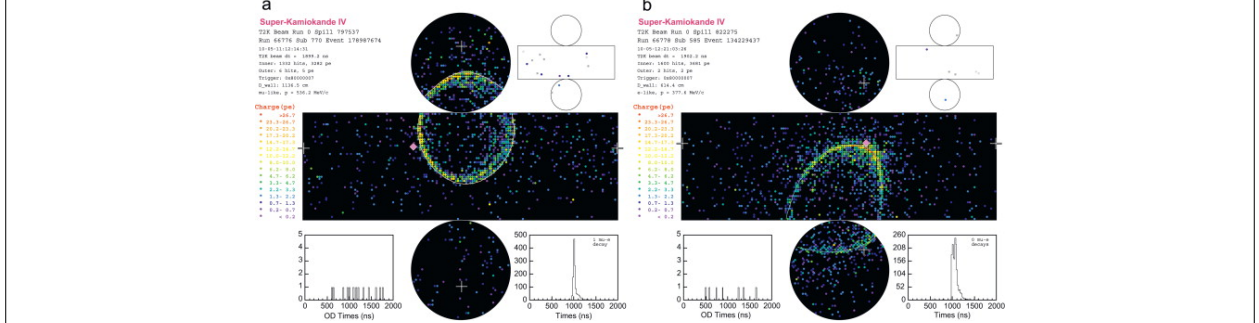


**Figure 1.27:** Representative T2K events in Super-Kamiokande for (a) a muon-like ring and (b) an electron-like ring. Both figures show Super-Kamiokande unrolled onto a plane with each colored point representing a PMT. The color of each PMT corresponds to the amount of charge collected. In upper right corner shows the same unrolled hit map for the veto outer detector. White crosses indicate the location of the reconstructed vertex. A solid diamond marks the location where a ray parallel to the beam would intersect the detector wall starting from the vertex.

Far Detector neutrino measurements. Therefore having some background on the oscillation analysis will illustrate ND280's utility and discussed in the next section.

#### 1.2.4 ND Constraint

As started before, the primary goals of T2K are measure to measure the oscillation parameters  $\theta_{13}$ ,  $\theta_{23}$ , and  $\Delta m_{23}^2$ . This is performed by fitting the oscillation parameters to the number of observed flavored neutrinos at SK. The number of reconstructed neutrino events of flavor  $\alpha$ ,  $N_{\nu_\alpha}$ , observed is

$$N_{\nu_\alpha} = B + S_{\nu_\alpha} \quad (1.55)$$

where  $B$  are all misidentified  $\nu_\alpha$  events and  $S_{\nu_\alpha}$  is the number of true events. The expected rate given by

$$S_{\nu_\alpha} = \sum_{\lambda=e,\mu} \left[ \mathcal{P}_{\nu_\lambda \rightarrow \nu_\alpha} (E_\nu; \vec{\sigma}) \right] \times \sum_t \left[ \sigma_{\nu_\alpha}^t (E_\nu) \cdot t_N \right] \\ \times \Phi_{\nu_\alpha} (E_\nu) \times \epsilon(p_\alpha, \theta_\alpha), \quad (1.56)$$

where  $\vec{\sigma}$  is a vector of the oscillation parameters from equation (??) equation (??),  $\sigma_{\nu_\alpha}^t$  is the cross section for  $\nu_\alpha$  on target  $t$ ,  $t_N$  is the number of targets of type  $t$ ,  $\Phi_{\nu_\alpha}$  is the flux

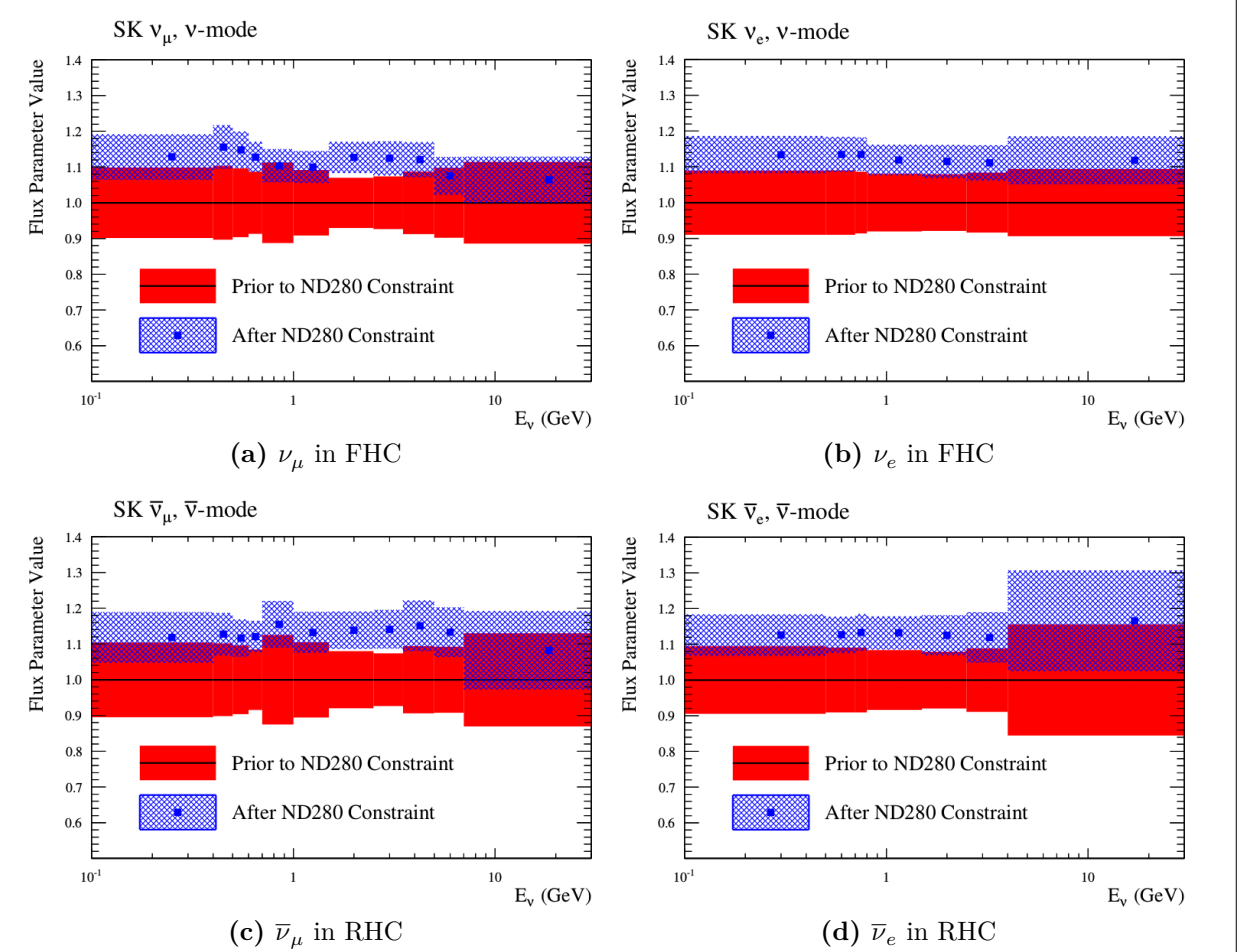


**Figure 1.28:** Predicted and best fit measurements for the SK flux. The horizontal axes are the neutrino energy and the vertical axes are the fractional change in the flux normalization. These figures were taken from the 2017 T2K oscillation analysis [4]. A value 1.1 corresponds to a 10% increase in the number of predicted events.

of neutrinos, and  $\epsilon(p_\alpha, \theta_\alpha)$  is the efficiency of reconstructing and correctly categorizing the event as a function of momentum  $p$  and angle  $\theta$ .

Having a large, sensitive ND like ND280 in line with beam provides critical constraints to the flux and cross sections in the oscillation analysis. Without ND280, the fractional uncertainty on the flux rate is about  $\sim 10\%$  per energy bin. Adding the ND constraint reduces the uncertainty to about  $\sim 5\%$  as seen in 1.28. There are numerous cross section channels that affect T2K's sensitivity to the oscillation parameters, with the most important being CCQE and CCQE-like interactions as shown in . At energies near the  $\nu_e$  appearance

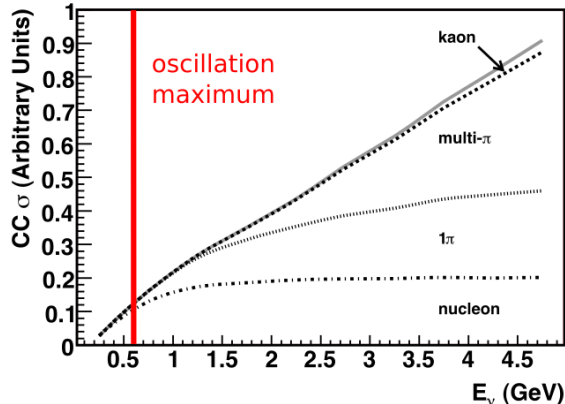


**Figure 1.29:** Predicted CC inclusive scattering cross section at T2K relevant energies. Only the most common final state modes are shown. A thick, red line indicates the T2K  $\nu_e$  appearance probability maximum. For CCQE-like interactions, they usually include the emission of nucleons. Resonance states and DIS interactions produce  $1\pi$ ,  $N\pi$  and kaon final states as well. Combined, the inclusive cross section increases linearly with energy. This image was edited and originally produced by Formaggio and Zeller [18]

probability maximum,  $E_\nu = 0.6$  GeV, the CCQE interaction is largest contributor to the inclusive cross section as shown in 1.29.

---

# Chapter 2

## BANFF Likelihood

The BANFF likelihood maximization procedure is a binned likelihood maximization fitting of the ND280 data. This is separate from the fitting the Super-Kamiokande (SK) data. In a joint fit, the measurements from both detectors are considered along with their respective nuisance parameters. This approach is more computationally expensive since the time to perform a fit increases non-linearly with increasing the number of fit parameters. However it is developed in an alternate method called the Markov Chain Monte Carlo analysis (MaCh3) and this will not be explained here. The BANFF likelihood maximization, hitherto referred to as the “BANFF-fit”, includes nuisance parameters that affect the measurement of the oscillation parameters, but are not physics goals of the T2K experiment. The BANFF-fit parameters and their respective covariances are then used as inputs in the oscillation analysis. This “divide-and-conquer” approach allows for more rapidly completed studies on the effects of model parameters and biases present. Also this approach should provide the same result with a joint ND280 and SK analysis as is performed in MaCh3. However, information encoded in the ND280 measurements for shared nuisance parameters like the neutrino flux is inevitably lost in the BANFF-fit.

The modern BANFF-fit likelihood is described in detail in detail in [Insert PRD instead](#) TN-220 [20]. It uses a frequentist approach to find the best nuisance parameter set to maximize a

---

binned likelihood. Subsequent updates to the BANFF-fit have increased the sample sizes and systematic parameterizations.

### 2.0.1 Motivation

Curve fitting is commonly found in the particle physics community literature due to the need to compare two models or constrain unknown model parameters using one or more histograms. For the first case, this involves two competing models,  $H_0$  and  $H_1$ , in order to establish if the data supports new Physics ( $H_1$ ) not predicted in the Standard Model ( $H_0$ ). The second case finds the “best” set of the model predictions,  $\theta$ , that match the data as is the case for the BANFF-fit. In both cases, chi-squared tests are performed to provide goodness of fit, parameter estimation (also referred to as “best fit parameters”), and error/confidence estimation.

### 2.0.2 Introduction to Conditional PDFs and Likelihoods

Consider the problem of extracting physics parameters  $\vec{y}$  given some data vector  $\vec{N}$ . The conditional probability density function (PDF)  $\mathcal{P}$  to measure these parameters is given as

$$\mathcal{P}(\vec{y}|\vec{N}) = \frac{\mathcal{L}(\vec{N}|\vec{y})\mathcal{P}(\vec{y})}{\int \mathcal{L}(\vec{N}|\vec{x})\mathcal{P}(\vec{x})d\vec{x}}, \quad (2.1)$$

where anything right of a vertical line represents a condition on the probability,  $\mathcal{L}(\vec{N}|\vec{y})$  is the likelihood of the model with parameters  $\vec{y}$ ,  $\mathcal{P}(\vec{y})$  is the probability for the model, and the denominator is the normalization over all possible constraints on the observations. A frequentist interpretation of a PDF is a proportion of outcomes of repeated trials or experiments. A likelihood function is an expression of the probability of observing data as a function of the model parameters in their appropriate ranges.

One arrives at (2.1) by using the definition of compound probabilities

---

$$\mathcal{P}(A, B) = \mathcal{P}(B|A)\mathcal{P}(A) \quad (2.2)$$

to evaluate  $\mathcal{P}(\vec{y}|\vec{N})$  as

$$\mathcal{P}\left(\underbrace{\vec{y}}_B \middle| \underbrace{\vec{N}}_A\right) = \frac{\mathcal{P}(\vec{N}, \vec{y})}{\mathcal{P}(\vec{N})} \quad (2.3)$$

with the denominator here is recognized as the normalization of the PDF. The compound PDF  $\mathcal{P}(\vec{N}, \vec{y})$  can expanded using Bayes' theorem which states

$$\mathcal{P}(A|B)\mathcal{P}(B) = \mathcal{P}(B|A)\mathcal{P}(A), \quad (2.4)$$

and combined with (2.2) yielding

$$\mathcal{P}\left(\underbrace{\vec{N}}_A, \underbrace{\vec{y}}_B\right) = \mathcal{P}(\vec{N}|\vec{y}) \times \mathcal{P}(\vec{y}), \quad (2.5)$$

where the PDFs to the left and right of the  $\times$  operator are recognized as the likelihoods and priors, respectively. Combining resulting in (2.3) and (2.5) reproduces the original expression of (2.1).

### 2.0.3 BANFF Fit Test Statistic

For the BANFF fit, one considers the problem of trying to maximize the agreement between measured and predicted data histograms. This is equivalent to maximizing a binned likelihood function  $\mathcal{L}$  of the data given the a set of parameters that predict the measured rate. The use of likelihood functions in fits to histogram is explained further in reference [9] and the PDG review on Statistics. By invoking Wilks' theorem, also known as the likelihood ratio theorem, the likelihood maximization procedure is converted into a minimization problem involving a test statistic denoted as a chi-squared. Below is an explanation of the BANFF test statistic,  $\Delta\chi^2$ , and its systematic model terms.

---

Consider many binned samples that select different charged current topologies. A convenient choice of observables for all the samples are the outgoing charged lepton  $l$  momentum  $P_l$  and angle  $\cos \theta_l$  as measured in ND280. Much of this is also documented in TN-220 [20] where additional details can be found. For each  $(P_l, \cos \theta_l)$  analysis bin  $i = 1, 2, \dots, M-1, M$ , the likelihood is given by

$$\mathcal{L}(\vec{N}^d | \vec{N}^p) = \left( \prod_{i=1}^M \left( \vec{N}_i^p \right)^{\vec{N}_i^d} \frac{e^{-\vec{N}_i^p}}{\vec{N}_i^d!} \right) \quad (2.6)$$

where  $\vec{N}_i^d$  is the number of observed data events in the  $i$ th bin and  $\vec{N}_i^p$  is the number of predicted events as a function of nuisance parameters in the  $i$ th bin. One recognizes the likelihood function in (2.6) as a product of Poisson distributions, since this is counting data measured in  $M$  analysis bins. The sets of dependent nuisance parameters, also sometimes called systematics, that affect the predicted event rate are

- cross section physics models, labeled as “xsec”,
- neutrino flux, and
- detector biases and inefficiencies.

Given these three sets of systematics, the number of predicted CC events from any neutrino flavor  $\nu_l$  at ND280 is calculated using the general formula

$$N_{\nu_l} = \underbrace{\Phi_{\nu_l}}_{\text{Flux per area}} \left[ \sum_t \underbrace{(\sigma_{\nu_l}^t M_t)}_{\text{Effective area}} \right] \underbrace{\epsilon_{\nu_l}}_{\text{Efficiency}} , \quad (2.7)$$

where  $\Phi_{\nu_l}$  is the flux of  $l$  flavor neutrinos,  $\sigma_{\nu_l}^t$  is the cross section of the interaction for neutrino flavor  $l$  on target  $t$ ,  $M_t$  is the number of  $t$  targets, and  $\epsilon_{\nu_l}$  is the total efficiency to reconstruct and properly identify the event as  $\nu_l$ CC interactions. Since the cross section is a measure of interaction probability in units of area, multiplication of  $M_t$  represents the effective cross sectional area of material  $t$  in the detector. Each term in (2.7) is modeled carefully and the

efficiency term is estimated using Monte Carlo (MC) simulations and control samples. The number of predicted events from the MC for a given analysis bin  $i$  is given by

$$\vec{N}_i^p(\vec{b}, \vec{x}, \vec{d}) = w_i^{\text{POT}} (\vec{d})_i^{\text{Det}} \sum_{j=1}^{N_i^{\text{MC}}} \left[ \sum_{k=1}^{N^{\text{Flux}}} \left( \delta_{j,k}^{\text{Flux}} (\vec{b})_k^{\text{Flux}} \right) \prod_{l=1}^{N^{\text{xSyst}}} w_{j,l}((\vec{x})_l^{\text{xsec}}) \right]. \quad (2.8)$$

Here  $w_i^{\text{POT}}$  is the protons on target (POT) weight for the  $i$ th analysis which normalizes the MC statistics to expected data statistics. To account for the detector inefficiencies, the  $(\vec{d})_i^{\text{Det}}$  parameters are normalization parameters that vary the total number of predicted events in the  $i$ th bin. Each  $(\vec{d})_i^{\text{Det}}$  is determined prior to the fit by surveying over a large number of toy experiments with the detector systematics varied in each. The sum over  $j = 1, 2, \dots, N_i^{\text{MC}} - 1, N_i^{\text{MC}}$  considers the contribution of all MC events in the  $i$ th analysis bin. The  $(\vec{b})_k^{\text{Flux}}$  parameters, out of a total of  $N^{\text{Flux}}$ , are flux normalization systematics for each flux bin. Since the flux bins are categorized not only by neutrino energy, but also by flavor and horn current, the  $\delta_{j,k}^{\text{Flux}}$  term in the sum over  $k$  selects the correct flux bin. The parameters  $w_{j,l}$  are pre-calculated weights as a function for the  $l$ th cross section model,  $(\vec{x})_l^{\text{xsec}}$ , with a total of  $N^{\text{xSyst}}$  cross section model terms. Different  $t$  target materials have separate cross section parameters. Also the number of targets  $M_t$  can vary via detector systematics.

Using the likelihood ratio test theorem, a test statistic is defined as taking -2 times the natural logarithm of the ratio of predicted to observed likelihoods

$$\Delta\chi_{\text{LLR}}^2 = -2 \log \frac{\mathcal{L}(\vec{N}^d | \vec{N}^p)}{\mathcal{L}(\vec{N}^d | \vec{N}^d)}, \quad (2.9)$$

where this test statistic  $\Delta\chi_{\text{LLR}}^2$  obeys a true chi-squared distribution for asymptotically large statistics and the likelihood functions are of the form (2.6). The denominator in (2.9) is the MC predicted probability which assumes the best maximum likelihood estimate is the number of observed events. Penalty terms from the cross section, flux, and detector

systematics are included in order to prevent overfitting of the data. The new test statistic for all of ND280,  $\Delta\chi^2_{\text{ND280}}$ , is given by

$$\begin{aligned}\Delta\chi^2_{\text{ND280}} &= \Delta\chi^2_{\text{LLR}} + \Delta\chi^2_{\text{xsec}} + \Delta\chi^2_{\text{Flux}} + \Delta\chi^2_{\text{Det}} \\ &\quad - 2 \left( \log \frac{\mathcal{L}(\vec{N}^d | \vec{N}^p)}{\mathcal{L}(\vec{N}^d | \vec{N}^d)} + \underbrace{\log \pi(\vec{x})}_{\text{xsec}} + \underbrace{\log \pi(\vec{b})}_{\text{Flux}} + \underbrace{\log \pi(\vec{d})}_{\text{Det}} \right),\end{aligned}\quad (2.10)$$

where each of the PDFs  $\pi(\vec{y} = \vec{x}, \vec{b}, \vec{d})$  are assumed multivariate normal distributions

$$\pi(\vec{y}) = C_y e^{(-\frac{1}{2}\Delta\vec{y} \cdot V_y^{-1} \cdot \Delta\vec{y}^T)}, \quad (2.11)$$

$\Delta\vec{y}$  is a vector with the difference between the current/explored and nominal set of vector parameters  $\vec{y}$ ,  $T$  corresponds to the transpose operator, and the normalization is given by

$$C_y = ((2\pi)^{k_y} \det(V_y))^{-\frac{1}{2}} \quad (2.12)$$

with  $V_y$  being the covariance matrix for a vector  $\vec{y}$  with  $k_y$  rows. The expanded form of the test statistic  $\Delta\chi^2_{\text{ND280}}$  is given by

$$\begin{aligned}\Delta\chi^2_{\text{ND280}} &= 2 \sum_{i=1}^M \left[ \vec{N}_i^p - \vec{N}_i^d + \vec{N}_i^d \log \left( \frac{\vec{N}_i^d}{\vec{N}_i^p} \right) \right] \\ &\quad + \Delta\vec{x} \cdot (V_x^{-1}) \cdot \Delta\vec{x}^T + \Delta\vec{b} \cdot (V_b^{-1}) \cdot \Delta\vec{b}^T + \Delta\vec{d} \cdot (V_d^{-1}) \cdot \Delta\vec{d}^T\end{aligned}\quad (2.13)$$

where the “ $\cdot$ ” is the matrix multiplication operator. It must be stated that the test statistic (2.13) purposefully *excludes normalization terms*. Once the global minimum of the test statistic is found, the postfit covariance matrix  $V$  is calculated as the inverse of the Hessian matrix  $H$

$$V_{i,j}(\hat{\vec{y}}) = (H_{i,j})^{-1} = \left( \frac{\partial^2}{\partial y_i \partial y_j} (\Delta\chi^2_{\text{ND280}}) \Big|_{\vec{y}=\hat{\vec{y}}} \right)^{-1} \quad (2.14)$$

where  $y_i, y_j \in \vec{y}$  and  $\hat{\vec{y}}$  is the maximum likelihood estimate for the parameters  $\vec{y}$ .

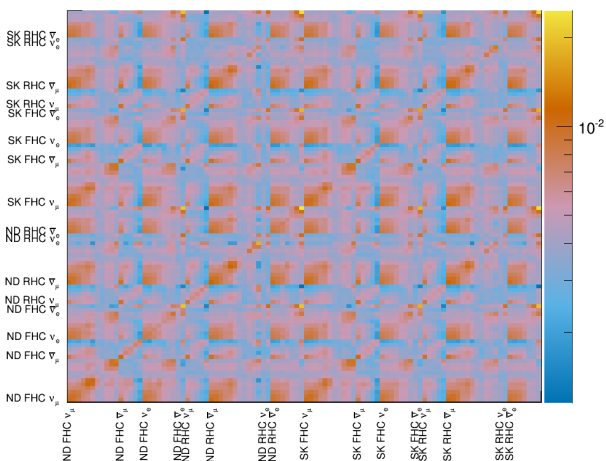


**Figure 2.1:** BANFF pre-fit flux covariance matrix shown with respective detector, horn current, and neutrino flavor.

### 2.0.3.1 Flux, Cross Section, and Detector Systematics

Below is a description for each of the systematics in the BANFF likelihood and test statistic penalty terms. First is a description of flux, followed by the cross section, and finally the detector systematics.

**Flux:** The flux weight is binned as a function of neutrino energy, horn current/polarity (FHC and RHC), and neutrino flavor ( $\nu_{\mu}$ ,  $\bar{\nu}_{\mu}$ ,  $\nu_e$ , and  $\bar{\nu}_e$ ). There are 50 ND280 and 50 SK parameters with an associated covariance matrix as shown in Figure 2.1. The binning and covariance matrix is provided by the T2K flux group prior to the BANFF analysis. Each flux bin is assigned a normalization parameter with initial value of one (1) for all events in that neutrino energy bin. A value of 1.1 indicates that any event in that energy bin has an additional weight of 1.1, or 10% increase in events. An example of the flux normalizations and uncertainties used in the 2017 analysis are shown in Figure 2.2.

**Cross Section:** There are a number of cross section model systematics implemented in BANFF to account for the uncertainties in cross section measurements. The cross section models used in this analysis are the 2017 Neutrino Interactions Working Group (NIWG) parameterization, which is a canonical set of parameters and covariance matrix shared among all analyses in T2K. A technical description of the 2017 parameterization is given in [insert](#)

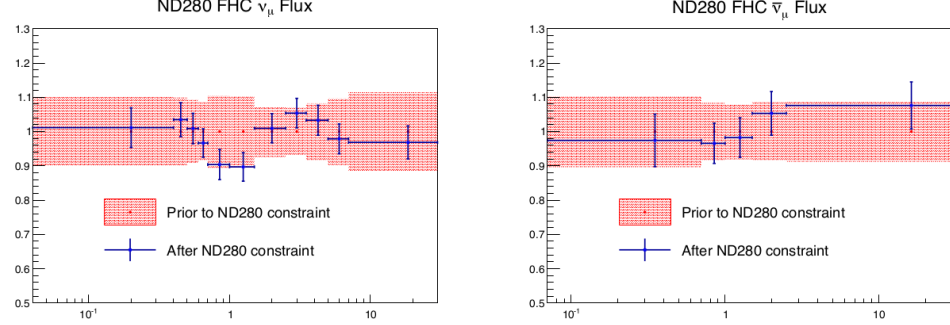


**Figure 2.2:** BANFF ND280 flux  $\nu_\mu$  and  $\bar{\nu}_\mu$  binning parameters from [Insert PRD ref](#) TN-324 data post-fit results. The uncertainties are extracted from the pre-fit and post-fit covariance matrices.

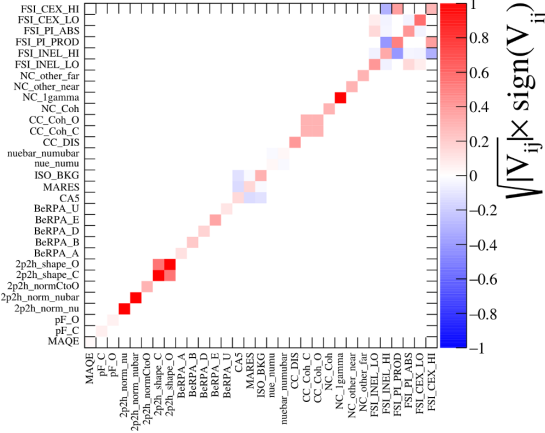


**Figure 2.3:** Cross section parameters pre-fit correlation matrix from the 2017 BANFF analysis.

[PRD ref](#) TN-315 [10] and TN-307 [25]. There are a total of 25 cross section parameters for interactions like meson exchange current that affect the shape and normalization of the cross section. The cross section correlation matrix is shown in Figure 2.3 [?].

**Detector Systematic Errors:** Detector systematics are implemented in BANFF to account for uncertainties in detector efficiencies. Since neutrino interaction events can migrate from sample-to-sample, bin-to-bin, or both depending on the relevant systematics, numerous toy experiments are performed by varying parameters that model known detector systematics.

After many toy experiments, a covariance matrix among the bins is constructed considering correlations and statistical errors. This detector covariance matrix is fractional to be consistent with the definitions for the flux and cross section covariance matrices. The

detector covariance matrix,  $\sigma_{\text{Det}}^2$ , between bins  $x$  and  $y$  given explicitly as

$$\sigma_{\text{Det}}^2(x, y) = \frac{1}{x_{\text{Nom}}} \frac{1}{y_{\text{Nom}}} (\sigma_{\text{Cov}}^2(x, y) + \sigma_{\text{Stat}}^2(x, y)), \quad (2.15)$$

where “Nom”, “Cov”, and “Stat” refer to the nominal MC prediction, covariance, and statistical uncertainties for bins  $x$  and  $y$ , respectively. The nominal bin expectation for bin  $x$  is

$$x_{\text{Nom}} = \sum_{k=1}^{N_x^{\text{MC}}} w_k, \quad (2.16)$$

where  $N_x^{\text{MC}}$  being the number of predicted MC events in the bin and  $w_k$  being the product of all the weights applied to the  $k$ th event (see (2.8) for all possible weights). The covariance and statistical terms are given by

$$\begin{aligned} \sigma_{\text{Cov}}^2(x, y) &= \frac{1}{N_{\text{Toy}}} \sum_{t=1}^{N_{\text{Toy}}} (x_t - \bar{x})(y_t - \bar{y}) \\ \sigma_{\text{Stat}}^2(x, y) &= \delta(x, y) \sum_{k=1}^{N_x^{\text{MC}}} w_k^2, \end{aligned} \quad (2.17)$$

where  $N_{\text{Toy}}$  is the number of toy experiments,  $\bar{x}$  is the mean of the all the toy experiments in bin  $x$ , and  $\delta(x, y)$  is the Kronecker delta function. Additional uncertainties like fake data contributions are added to the covariance in quadrature.

While there could be one detector systematic normalization for each analysis bin, also called a observable normalization, a single one can be assigned to multiple analysis bins to reduce the number of fit parameters. This procedure requires careful consideration of the shared detector systematics among analysis bins. A considerable drawback to designing normalizations in this way is that not all detector systematics are Gaussian with respect to the observables ( $P_l, \cos \theta_l$ ), and so the covariance matrix is not an exact representation of the detector systematics.

---

# Chapter 3

## PØD Selections and Samples

This section describes the development of  $\nu_\mu$  and  $\bar{\nu}_\mu$  CC Inclusive selections in both FHC and RHC beam configuration for PØD-based analyses. These selections are the continuation of previous works that developed  $\nu_\mu$  CC Inclusive selections between the PØD and TPC1. The first such analyses were T2K-TN-80 and T2K-TN-100 which described the  $\nu_\mu$  CC Inclusive event selection and, later, cross-section analysis using ND280 Production 5 software, respectively [?, 14]. These analyzes relied on each sub-detector’s reconstruction software and developed a track matching algorithm since the ND280 “Global” reconstruction matching was problematic in Production 5. As the inter-detector matching reconstruction improved in “Global”, two CC- $0\pi$  cross section analyzes, T2K-TN-258 and T2K-TN-328, were developed that also used the CC Inclusive selection as pre-selection cuts [?, ?]. The selections described in this technical note also employ the same pre-selection cuts. What follows from here in this section is a layout of the following topic discussions.

The first topic discussed in this section is a description of the  $\pi^0$  Detector (PØD). The next topic is the event reconstruction using the “Global” reconstruction software. Following that is the pre-selection cut flow. With the pre-selection cuts established, each of the three CC Inclusive selection’s cut flow is described. Concluding this section is a discussion of the

---

three samples in the following order:  $\nu_\mu$  in FHC mode,  $\bar{\nu}_\mu$  in RHC, and  $\nu_\mu$  background in RHC.

### 3.1 Global Reconstruction

The task of the Global reconstruction is to combine all the ND280 information into a combined reconstructed object. It was originally designed to analyze “CCQE-like” events in the Tracker region and has been extended to operate with all of ND280. A brief description of the Global reconstruction is described below. First the specific detector technologies and electronics of ND280 are explained. That is followed by the calibration procedure to properly tune each detector’s response. And finally a general outline of the reconstruction algorithms to form tracks and vertices in ND280 is presented.

ND280 events are first collected in the form of electronic signals from either multipixel photon counters (MPPCs) in the scintillator-based sub-detectors or charge collection planes of the time projection chambers (TPCs). MPPCs were chosen for the scintillator-based sub-detectors since they are insensitive to the strong 0.2T magnetic field present in ND280. The PØD, ECals, and SMRD all share the same “Trip-T” frontend board (TFB) electronics of which collect the photoelectrons released when photons interact with a pixel in the MPPCs. The FGDs operate with the same MPPC technology while using different frontend electronics. The TPCs utilize a locally strong electric field to collect ionization electrons from an Argon-based gas. Collected charge in the TPCs are collected and enhanced using micromega technology [1]. With the collected information from each sub-detector, the next step is the data calibration.

Data calibration in ND280 is the process where the charge and timing information collected from each sub-detector is adjusted to match with expected parameters. This is an important process that takes into account environmental changes, aging effects, and other behavior that might be present. Calibration data is collected frequently before and during

---

operational runtime and is stored in a database for later use. A common calibration is to measure the detector’s cosmic ray response since most cosmic rays deposit the same energy per unit length. After the data has been calibrated, reconstruction algorithms now attempt to find charged particle tracks in the data.

The Global reconstruction is a software package that attempts to recognize patterns of data to form tracks and find vertices for those tracks. Particle shower reconstruction in Global will not be discussed in this TN since no shower objects are used. Each sub-detector reconstruction is run to seeds Global’s track matching algorithms. Global attempts to then re-fit sub-detector tracks using a Kalman filter while correcting for particle energy loss as a function of length ( $dT/dx$ ) and multi-scattering processes. A vertex is then associated with the re-fit track using another Kalman filter algorithm. A further detailed description of the track matching and vertex finding algorithms for Global is described in T2K-TN-46 [?].

## 3.2 PØD Selection Cuts

The selection of CC Inclusive events use a series of cuts to select the primary lepton. The pre-selection cuts (“precuts”) are applied first to extract events that start in the PØD FV. A MIP is more likely to reach TPC1 from the PØD FV since the PØD is constructed out of heavy materials especially in the CECal. So the main track each selection is designed to select a muon.

This following sections will describe the precuts common to all CC Inclusive selections and the branching of different cuts, after the precuts, to select the main track.

### 3.2.1 Pre-Selection Cuts

The pre-selection (“precuts”) were initially developed to select  $\nu_\mu$ CC Inclusive using the PØD and TPC sub-detector reconstruction softwares separately [?]. They were then used with the Global reconstruction software for the  $\nu_\mu$ CC- $0\pi$  selection in the FHC beam

---

configuration as described in technical note T2K-TN-258 [?]. The description and flow of the precuts are described here as well since there is an incomplete description of the selection precuts.

The precuts are performed on each bunch per beam spill as follows

1. The event has a “good” data quality flag.
  - An event is rejected if any sub-detector or electronics in ND280 reported as “bad” during that bunch.
2. There is at least one (1) track reconstructed in TPC1.
  - There are no restrictions on the number of tracks fully contained in the PØD or exiting into other sub-detectors.
3. The track in TPC1 must have more than 18 nodes.
  - The TPC reconstruction gathers vertical and horizontal hits into clusters of hits. The charge distribution of the cluster is used to get a vertical (horizontal) position that is more accurate than the individual readout pads. A node is constructed out of each cluster with associated track state information. The set of nodes are used to fit the track helix [21].
4. The reconstructed vertex is within the PØD WT FV.
  - The PØD FV is defined to include as much as the WT regions as possible. Its X and Y borders are 25 cm away from the PØDule edges while its Z borders intersect the last and first half downstream PØDule in the USECal and CECal, respectively. The enumerated volume edges are shown in table 3.1. This volume, while used for track-based analyzes in the past, was optimized for  $\pi^0$  and  $\nu_e$  analyzes [?].
5. All tracks that enter TPC1 pass the veto cut

- An event is rejected if any PØD track enters TPC1 from outside the “corridor” volume. This cut was designed to eliminate broken tracks between the PØD and TPC1 when the separate sub-detector reconstructions were used [?]. In practice, this cut ensures that Global tracks entering TPC1 away from its X and Y edges. The corridor definition is the same as defined in T2K-TN-208 and shown in Table 3.1.

PØD WT FV			Corridor Volume		
-836	$< X <$	764	-988	$< X <$	910
-871	$< Y <$	869	-1020	$< Y <$	1010
-2969	$< Z <$	1264	-3139	$< Z <$	-900

**Table 3.1:** The PØD WT FV (left) and veto corridor volume (right) in the ND280 coordinate system. The corridor spans from the 5th (8th) to 40th (80th) PØDule (scintillator layer). All the units are given in millimeters.

After passing all the precuts, a single, global track, which is observed in TPC1, is assigned as the lepton candidate or “main track” of a selection.

The momentum of the main track,  $P$ , is sum of its momentum in the TPC,  $P_{\text{TPC}}$ , with the estimate momentum lost in the PØD,  $\Delta P_{\text{PØD}}$

$$P = P_{\text{TPC}} + \Delta P_{\text{PØD}}. \quad (3.1)$$

Momentum lost in the PØD is estimated by summing the energy loss ( $dT/dx$ ) in along the track path  $dx$

$$\Delta T = \int \left( \frac{dT}{dx} \right) dx. \quad (3.2)$$

Using the chain rule, we can convert the energy loss into momentum loss

$$\begin{aligned}
\frac{dT}{dx} &= \left( \frac{dT}{dP} \right) \left( \frac{dP}{dx} \right) \\
&= \left( \frac{Pc^2}{E} \right) \left( \frac{dP}{dx} \right) \\
&= \beta c \left( \frac{dP}{dx} \right),
\end{aligned} \tag{3.3}$$

where  $\beta$  is the particle velocity as a ratio of the speed of light  $c$ . The fundamental theorem of Calculus permits us to write the energy loss now as a momentum loss

$$\Delta P_{\text{P}\emptyset\text{D}} = \int \left( \frac{dP}{dx} \right) dx = \frac{1}{c} \int \left[ \left( \frac{dT}{dx} \right) \frac{1}{\beta} \right] dx.$$

Since we cannot take infinitesimally small steps along the track, we must replace the integral with a sum and  $dx \rightarrow \Delta x$  to arrive at the expression of the momentum loss estimate in the PØD

$$P = P_{\text{TPC}} + \frac{1}{c} \sum_t \left[ \left( \frac{dT}{dx} \right) \left( \frac{\Delta x}{\beta} \right) \right]_t. \tag{3.4}$$

For most tracks entering the TPC, they will be highly relativistic in the PØD ( $\beta(x) \approx 1$ ), and (3.4) becomes

$$P = P_{\text{TPC}} + \frac{1}{c} \sum_t \left[ \left( \frac{dT}{dx} \right) \Delta x \right]_t \tag{3.5}$$

The next sections describe the selection cuts, first in FHC mode and then RHC mode.

### 3.2.2 $\nu_\mu$ CC Inclusive in FHC Cut

- The highest momentum negatively charged track (HMNT) is the lepton candidate

As discussed in Section 3.2.1 on page 57, this selection is the basis for the  $\nu_\mu$  CC-0 $\pi$  PØD+TPC1 analysis. In FHC mode, the vast majority of neutrino interactions are  $\nu_\mu$ CC events producing an outgoing, negatively charged muon. So if there is no negatively charged track in the TPC, the event is rejected.

---

### 3.2.3 $\bar{\nu}_\mu$ CC Inclusive in RHC Cuts

- The highest momentum positively charged track (HMPT) is the lepton candidate
- The HMPT must be the highest momentum track (HMT)

In RHC, the majority of neutrinos in the beam is  $\bar{\nu}_\mu$  since the horn focuses negatively charged pions. To select  $\bar{\nu}_\mu$  CC interaction events by selecting positively charged muons, the lepton candidate is the HMPT in the TPC. The event is rejected if there is no positively charged track. However, since the RHC mode beam is not as  $\bar{\nu}_\mu$  pure as the FHC beam, another cut was added to reduce this effect.

Since RHC neutrino beam can be described as a  $\bar{\nu}_\mu$ -enhanced beam, the HMPT must also be the HMT due to the significant “wrong-sign”  $\nu_\mu$  background. This effect is two fold due to the nature of the neutrino source and the cross section between neutrinos and antineutrinos. Firstly the neutrino flux is larger in RHC mode due to neutrino production at the target. The source of neutrinos are from protons, which have positive charge, on a graphite target. This method is more likely to produce positively charged pions in the target than negatively charged one. While the horns are designed to select the negatively charged pions in RHC mode, the excess amount of positively charged pions will penetrate the horns’ filter. Therefore there are many more  $\pi^+ \rightarrow \mu^+ + \nu_\mu$  decays in RHC compared to FHC mode. Secondly, antineutrino interactions on matter are suppressed compared to neutrinos due to helicity considerations as explained in 1.1.1.3 on page 11.

### 3.2.4 $\nu_\mu$ Background CC Inclusive in RHC Cuts

- The highest momentum negative track (HMNT) is the lepton candidate
- The HMNT must be the highest momentum track (HMT)

As discussed in 3.2.3, the RHC neutrino beam has a significant wrong-sign  $\nu_\mu$  background. The selection of the HMNT is designed to select the negatively charged muons. To prevent

---

selecting the antineutrino events, the HMNT must also be the HMT. The event is rejected if there is no negatively charged track. If there are both positively and negatively charged tracks, the HMT cut discriminates if the event originates from a  $\nu_\mu$  or  $\bar{\nu}_\mu$ .

### 3.3 Selection Kinematics

This section examines the kinematics for each of selections while differentiating between water-in and water-out mode. The selection cuts were implemented in Psyche which is the software interface that BANFF uses to select events. The data sets used in this analysis are runs 2-8 in both PØD water-in and water-out (air) modes as shown in Table ??.

#### 3.3.1 $\nu_\mu$ FHC CC 1-Track

This selection provides the CCQE-like samples in FHC mode. 3.1 on the next page display the momentum and angular distributions that are inputs to BANFF. In the majority of cases, the lepton candidate is the true muon. The underlying true kinematics,  $E_\nu$  and  $Q^2$ , of the interactions are shown in 3.2 on page 64 which are of theoretical importance in the cross section and flux models.

An interesting CCQE-like topology in this selection are “2 particle 2 hole” (2p2h) events where neutrino scatters off a correlated (aka nearby and interacting) nucleon pair. Interaction model for 2p2h are included the BANFF fit whose model uncertainties are quite large in T2K.

This selection contains a modest fraction of non-CCQE interactions. The largest contamination is single pion interactions ( $1\pi$ ), which can happen for a number of reasons. First when the final state pion is produced, it is subject to final state interactions (FSI) where a pion can be absorbed or scatter in or out of the nucleus. In addition, a pion might not be reconstructed as a track in the PØD if its energy is below reconstruction threshold.

Add comparison between p0d CC-0pi paper and this analysis for validation. Include 2D numu CCQE efficiency and purity from HL2.

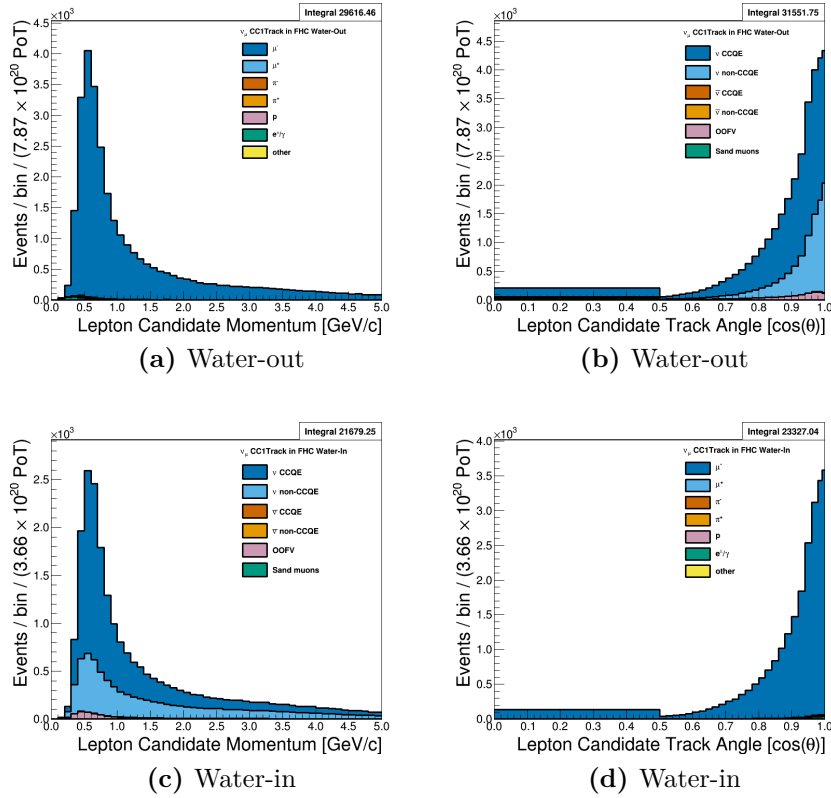


**Figure 3.1:**  $\nu_\mu$  in FHC CC 1-Track in  $P$  and  $\cos\theta$  distributions broken down by true NEUT interaction modes. The top figures (a) and (b) are for PØD water-out mode. The bottom (c) and (d) figures are PØD water-in mode. Each distribution is normalized to the FHC POT collected between run periods 2 - 8.

### 3.3.2 $\nu_\mu$ FHC CC N-Tracks

This selection provides non-CCQE samples in FHC mode inputs to BANFF. The reconstructed momentum and angular distributions are shown in 3.3 on page 65. Since this selection is not optimized for any particular CC topology, there are a variety of interactions modes present including  $1\pi$ , multiple pion ( $N\pi$ ) and deep inelastic scattering (DIS). There are a number of mis-identified lepton candidates in the form of electrons and pions.

The fundamental kinematics of the selection are shown in 3.4 on page 66. The selection captures the high energy tail of the neutrino flux which is relatively  $\nu_\mu$ -pure. True kinematics that describe the  $1\pi$ ,  $N\pi$ , and DIS models are parameterized in  $Q^2$  and the hadronic system mass  $W$ . The invariant  $W$  is defined as

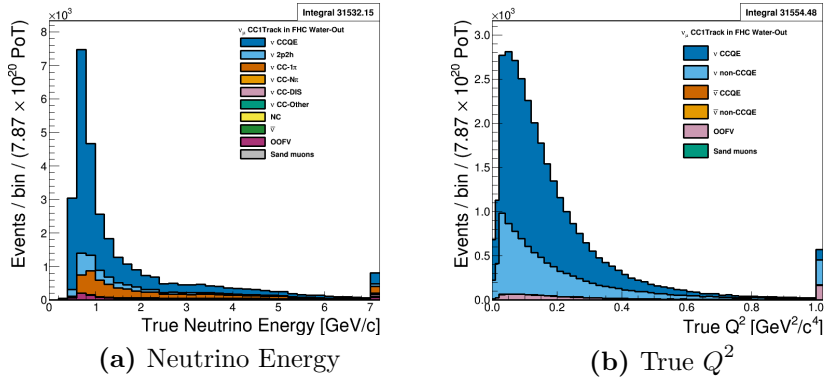


**Figure 3.2:**  $\nu_\mu$  in FHC CC 1-Track true  $E_\nu$  and  $Q^2$  distributions broken down by true NEUT interaction modes. Water-out mode is displayed here only with the last bin shown as overflow.

$$W^2 = M_N^2 + 2M_N(E_\nu - E_l) - Q^2, \quad (3.6)$$

where  $M_N$  is the mass of the struck nucleon and  $E_l$  is the energy of the outgoing lepton. A dominant mode in the selection are  $1\pi$  events from a  $\Delta$  resonance which has a rest mass of  $1.232 \text{ GeV}/c^2$ . The  $\Delta$  resonance is clearly seen in the  $W$  distribution in 3.4 on page 66. Higher order resonance states are present as well. **Add 2D eff and purity numu CC-Inclusive plots from HL2.**

### 3.3.3 $\bar{\nu}_\mu$ RHC CC 1-Track

This selection provides the  $\bar{\nu}_\mu$  CCQE-like samples in RHC mode that are inputs to BANFF. 3.5 on page 67 below display the momentum and angular distributions. The OOFV background tracks are mostly high momentum protons reaching into the TPC. The underlying true kinematics,  $E_\nu$  and  $Q^2$ , of the interactions are shown in figure 3.6. We see this is a  $\bar{\nu}_\mu$ -pure selection with a mixture of 2p2h and  $1\pi$  events similar to the results previously seen in section 3.3.1.

**Insert 2D efficiency and purity numubar CCQE efficiency plots from HL2.**

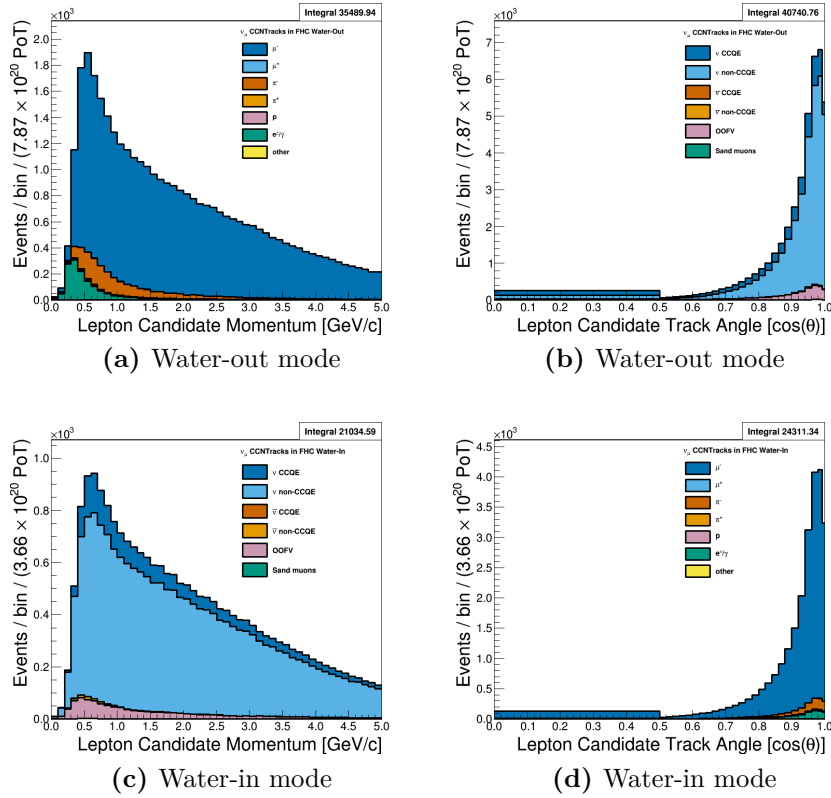


**Figure 3.3:**  $\nu_\mu$  FHC CC N-Tracks  $P$  and  $\cos \theta$  distributions broken down by true NEUT interaction modes. The top figures (a) and (b) are water-out mode. The bottom (c) and (d) figures are water-in mode. Each distribution is normalized to the FHC POT collected between run periods 2 - 8.

### 3.3.4 $\bar{\nu}_\mu$ RHC CC N-Tracks

This selection provides the non-CCQE-like samples in RHC mode. Figures below display the momentum and angular distributions that are inputs to BANFF. The underlying true kinematics,  $E_\nu$ ,  $Q^2$ , and  $W$  of the interactions are shown below.

Insert 2D efficiency and purity numubar CC-Inc plots from HL2. This means the flavor MUST be numubar.

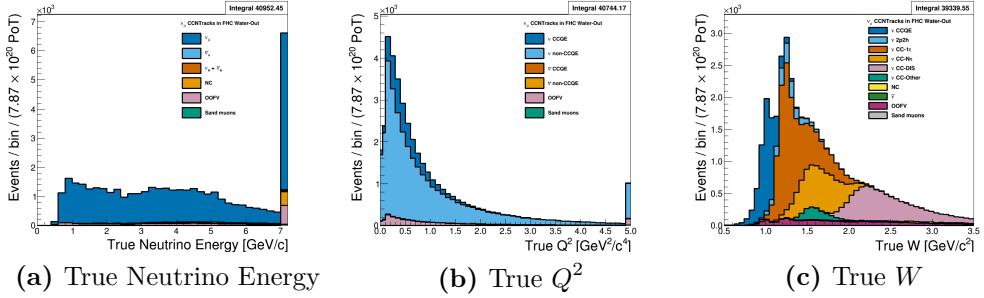


**Figure 3.4:**  $\nu_\mu$  FHC CC N-Tracks true kinematics broken down by true NEUT interaction modes. Sub-figures (a), (b), and (c) show the true neutrino energy,  $Q^2$ , and  $W$  distributions, respectively. Water-out mode is displayed here only with the last bin used as overflow is shown in (a) and (b).

### 3.3.5 $\nu_\mu$ Background in RHC CC 1-Track

This selection provides the wrong-sign ( $\nu_\mu$ ) background CCQE-enriched samples in RHC mode. Figures below display the momentum and angular distributions that are inputs to BANFF. The underlying true kinematics,  $E_\nu$  and  $Q^2$ , of the interactions are shown below.

Insert 2D efficiency and purity numu CCQE plots from HL2. This means the flavor MUST be numu.

### 3.3.6 $\nu_\mu$ RHC CC N-Tracks

This selection provides the  $\nu_\mu$  background non-CCQE-like samples in RHC mode. Figures below display the momentum and angular distributions that are inputs to BANFF. The underlying true kinematics,  $E_\nu$ ,  $Q^2$ , and  $W$  of the interactions are shown below.

Insert 2D efficiency and purity numu CC-Inc plots from HL2. This means the flavor MUST be numu.

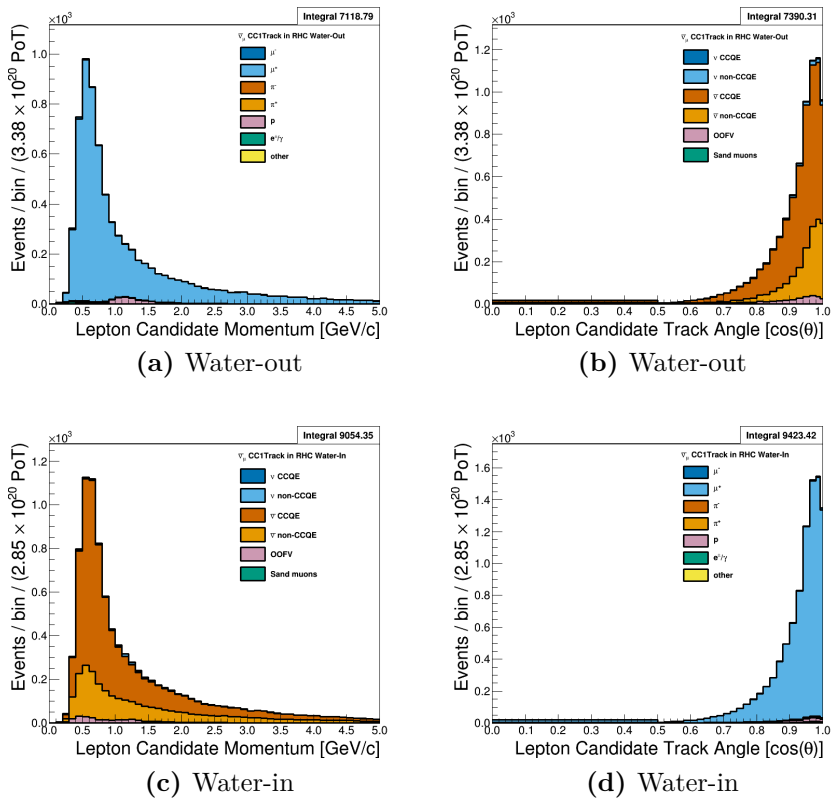


**Figure 3.5:**  $\bar{\nu}_\mu$  in RHC CC 1-Track  $P$  and  $\cos \theta$  distributions broken down by true NEUT interaction modes. The top and bottom figures are water-out and water-in mode, respectively.

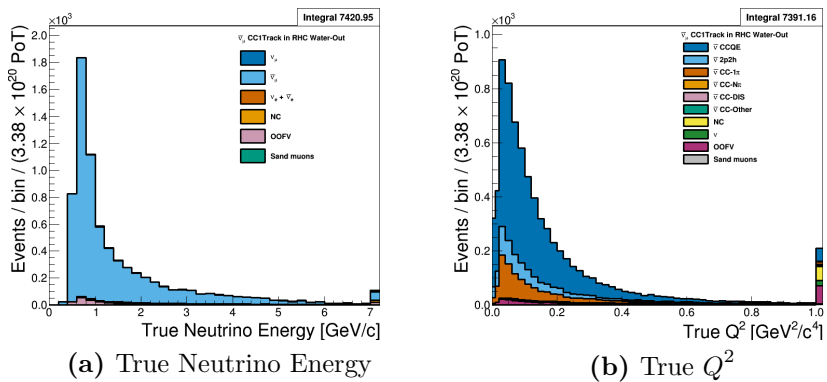


**Figure 3.6:**  $\bar{\nu}_\mu$  in RHC CC 1-Track true  $E_\nu$  and  $Q^2$  distributions. Sub-figure (a) is broken down by true neutrino flavor with (b) broken by more specific NEUT interaction modes. Water-out mode is displayed here only with the last bin used as overflow.

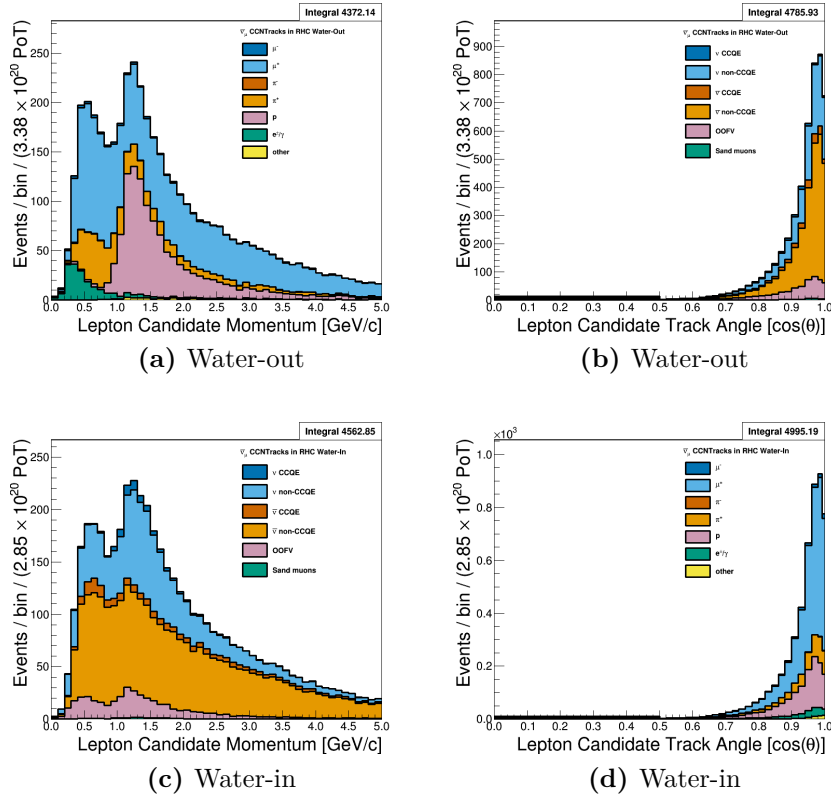


**Figure 3.7:**  $\bar{\nu}_\mu$  RHC CC N-Tracks  $P$  and  $\cos \theta$  distributions broken down by true NEUT interaction modes. The top and bottom figures are water-out and water-in mode, respectively.

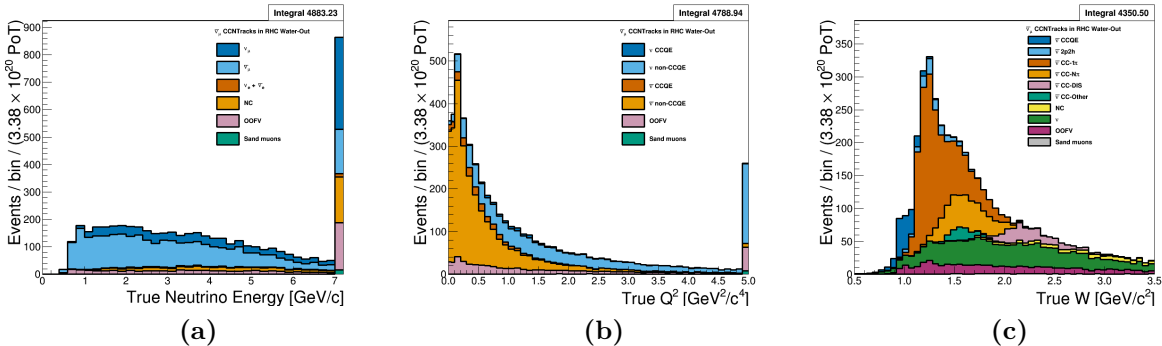


**Figure 3.8:**  $\bar{\nu}_\mu$  in RHC CC N-Tracks  $E_\nu$ ,  $Q^2$ , and  $W$  distributions broken down by true NEUT interaction modes.

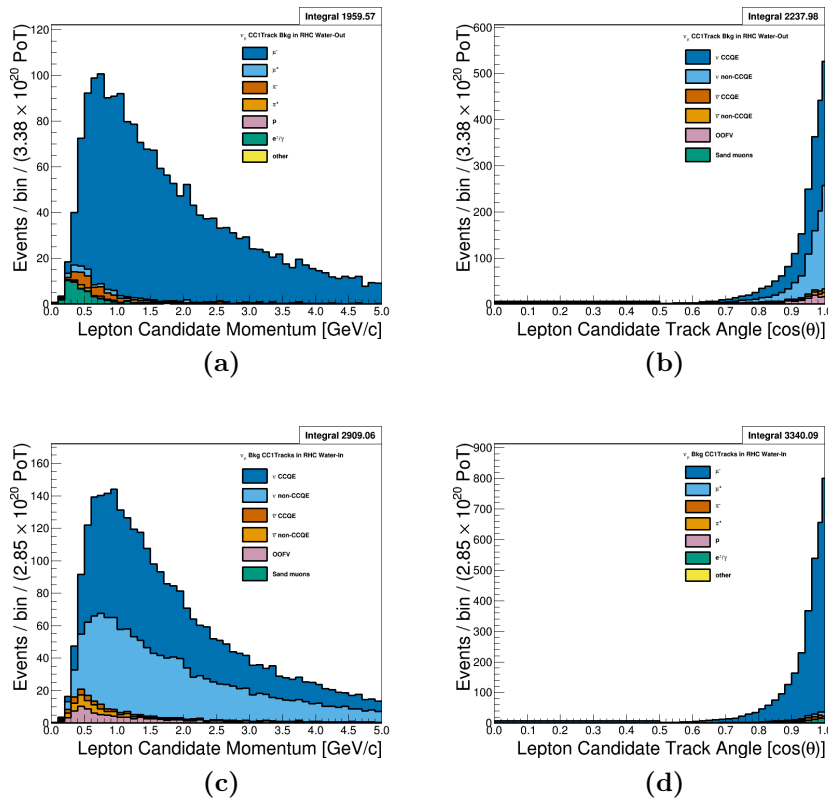


**Figure 3.9:**  $\nu_\mu$  in RHC CC 1-Track  $P$  and  $\cos\theta$  distributions broken down by true NEUT interaction modes. The top and bottom figures are water-out and water-in mode, respectively.

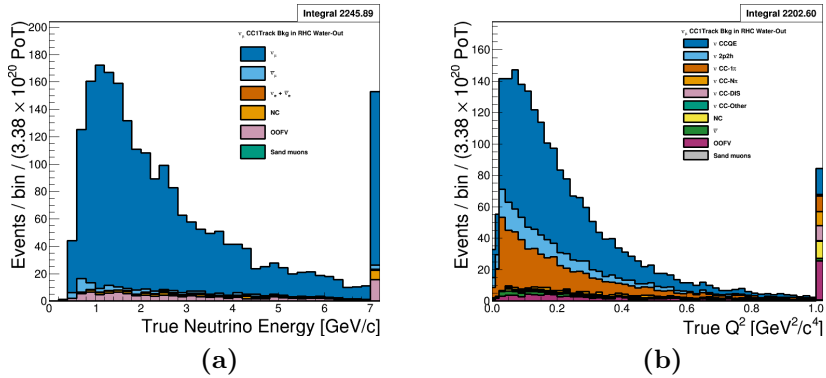


**Figure 3.10:**  $\nu_\mu$  in RHC CC 1-Track  $E_\nu$  and  $Q^2$  distributions. Sub-figure (a) is broken down by true neutrino flavor with (b) broken by more specific NEUT interaction modes.

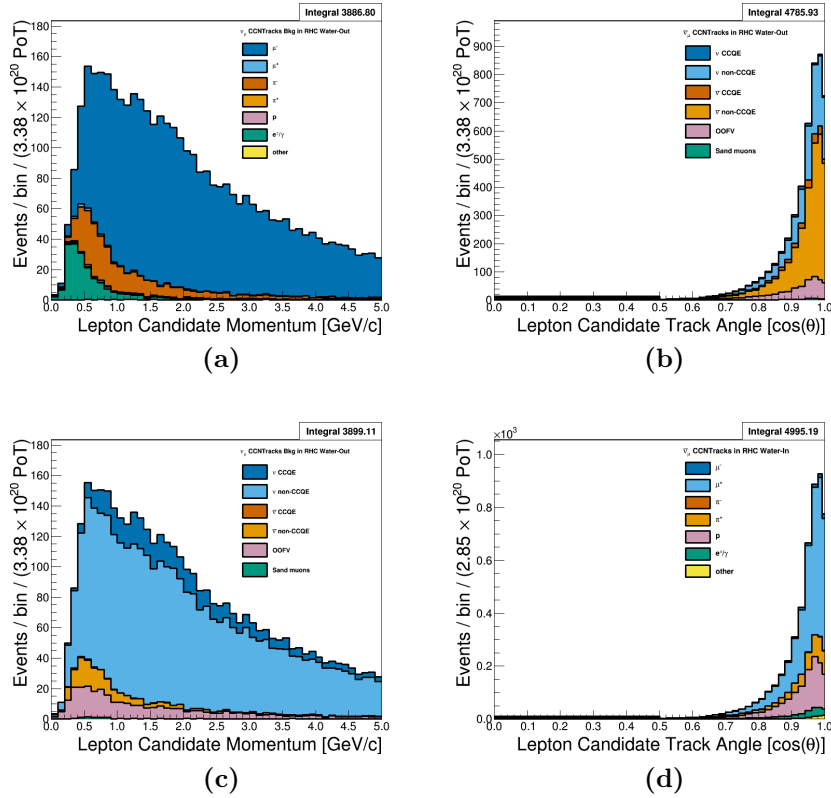


**Figure 3.11:**  $\nu_\mu$  RHC CC N-Tracks  $P$  and  $\cos\theta$  distributions broken down by true NEUT interaction modes. The top and bottom figures are water-out and water-in mode, respectively.

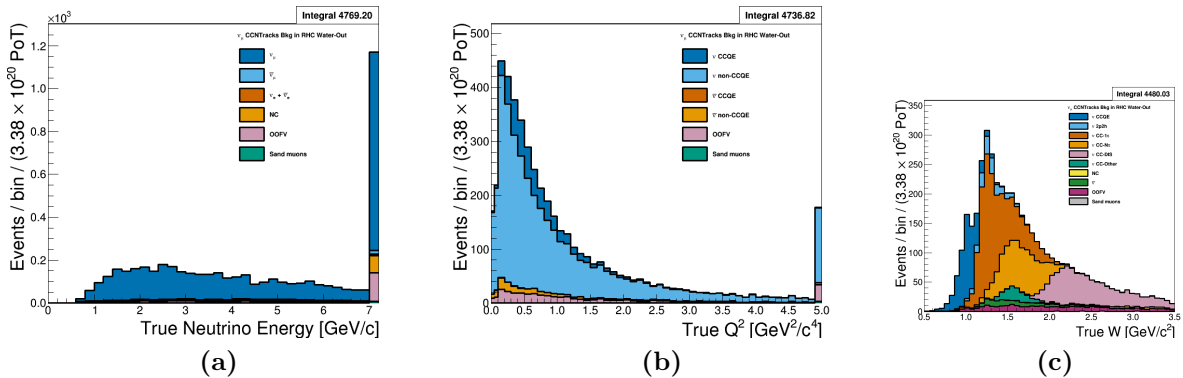


**Figure 3.12:**  $\bar{\nu}_\mu$  in RHC  $E_\nu$  and  $Q^2$  distributions broken down by true NEUT interaction modes.

---

# Chapter 4

## Systematic Uncertainties

Sources of systematic uncertainties, hitherto referred to as systematics, must be evaluated in order to understand their effect on any analysis. The BANFF fit utilizes a set of canonical systematics

### 4.0.1 Detector Systematic Uncertainties

All the detector systematics in BANFF are evaluated as either observable variations or weights. An observable variation affects the physical observables of selected events. The most important variation is the energy loss in the PØD of the outgoing muon in CC interactions.

#### 4.0.1.1 Efficiency-like Systematics

Efficiency-like systematics are treated as weights to the MC predictions in order to evaluate the uncertainty the systematic has on an analysis. They are based on studies comparing data and MC predictions in well known control samples (CS). A CS is designed to provide a reliable measurement with minimal influence from other dependent and independent factors. An example of a well established CS is a collection of single, isolated cosmic ray (muon) tracks to measure the energy loss in a detector. In general, a CS may have different properties than the analysis sample like event topology. In particular the cosmic ray CS

---

cannot account for efficiency effects of other tracks present. Therefore a model extrapolation is needed to map the CS to the analysis sample. The model used in psyche/BANFF is that the efficiency of the data and MC is the same in both analysis sample and CS

$$\epsilon_{\text{Data}}(o) = \left( \frac{\epsilon_{\text{Data}}(o)}{\epsilon_{\text{MC}}(o)} \right)_{\text{CS}} \epsilon_{\text{MC}}(o)$$

where  $\epsilon_{\text{MC}}/\epsilon_{\text{Data}}$  denotes the mean efficiency of the MC/data as a function of some observable  $o$ . We need to update this model to account for statistical uncertainties in the CS. The updated model, with  $o$  dependence assumed, is now

$$\epsilon'_{\text{Data}} = \left( \frac{\epsilon_{\text{Data}} + x_{\text{Data}} \cdot \sigma_{\epsilon_{\text{Data}}}}{\epsilon_{\text{MC}} + x_{\text{MC}} \cdot \sigma_{\epsilon_{\text{MC}}}} \right)_{\text{CS}} \epsilon_{\text{MC}}$$

where  $\sigma_{\epsilon_{\text{MC/}}\text{Data}}$  is the standard deviation of the efficiency of the MC/Data and  $x_{\text{Data}}$  and  $x_{\text{MC}}$  are different random, normally distributed numbers  $\mathcal{N}(\mu = 0, \sigma^2 = 1)$ .

$$w_{\text{eff}} = \frac{\epsilon'_{\text{Data}}}{\epsilon_{\text{MC}}}$$

$$w_{\text{ineff}} = \frac{1 - \epsilon'_{\text{Data}}}{1 - \epsilon_{\text{MC}}}$$

#### 4.0.1.2 Observable Variation Systematics

$$o' = o_{\text{Nom}} + \overline{\Delta o} + x\sigma_{\Delta o},$$

where  $o'$  is the varied observable value,  $o_{\text{Nom}}$  is the nominal MC value,  $\overline{\Delta o}$  is the average correction to the observable,  $\sigma_{\Delta o}$  is the uncertainty on the correction, and  $x$  is a random number from  $\mathcal{N}(\mu = 0, \sigma^2 = 1)$ .

#### 4.0.1.3 Normalization Systematics

Systematic effect	Treatment
TPC cluster eff.	efficiency
TPC tracking eff.	efficiency
TPC charge misassignment	efficiency
TPC momentum resol.	observable variation
TPC momentum scale	observable variation
B field distortion	observable variation
Pion secondary interactions	efficiency
Proton secondary interactions	efficiency
PØD energy loss scale	observable variation
PØD energy loss resol.	observable variation
PØD OOFV	efficiency
PØD track veto	efficiency

**Table 4.1:** [?]

$$w = w_0 (1 + x\sigma_w)$$

# Chapter 5

## PØD in BANFF Parameterization

### 5.0.1 PØD Samples Fit Binning

The PØD ND280 BANFF fit uses the samples described in ???. The bin edges are tabulated below.

- FHC  $\nu_\mu$ CC 1-Track bin edges:

$p$  [GeV/c]: 0, 0.3, 0.4, 0.5, 0.6, 0.7, 0.8, 1, 1.25, 1.5, 2, 3, 4, 5.5, 30

$\cos\theta$  : -1, 0.7, 0.8, 0.88, 0.94, 0.96, 0.975, 0.99, 1

- FHC  $\nu_\mu$ CC N-Tracks bin edges:

$p$  [GeV/c]: 0, 0.4, 0.5, 0.6, 0.7, 0.8, 1, 1.2, 1.5, 1.8, 2.2, 2.7, 3.5, 5, 10, 30

$\cos\theta$  : -1, 0.65, 0.77, 0.85, 0.9, 0.94, 0.97, 0.99, 1

- RHC  $\bar{\nu}_\mu$ CC 1-Track bin edges:

$p$  [GeV/c]: 0, 0.4, 0.5, 0.6, 0.7, 0.8, 1, 1.25, 1.5, 2, 3, 30

$\cos\theta$  : -1, 0.82, 0.87, 0.9, 0.93, 0.95, 0.97, 0.99, 1

- RHC  $\bar{\nu}_\mu$ CC N-Tracks bin edges:

$p$  [GeV/c]: 0, 0.5, 0.9, 1.25, 1.6, 2, 3, 8, 30

---

---

$\cos \theta$  : -1, 0.8, 0.89, 0.95, 0.97, 0.99, 1

- RHC  $\nu_\mu$ CC 1-Track bin edges:

$p$  [GeV/c]: 0, 0.4, 0.6, 0.8, 1.1, 2, 10

$\cos \theta$  : -1, 0.78, 0.84, 0.89, 0.92, 0.95, 0.97, 0.98, 0.99, 1

- RHC  $\nu_\mu$ CC N-Tracks bin edges:

$p$  [GeV/c]: 0, 0.4, 0.6, 0.8, 1, 1.5, 2, 3, 10

$\cos \theta$  : -1, 0.7, 0.8, 0.85, 0.9, 0.94, 0.965, 0.98, 0.99, 1

#### 5.0.1.1 Fit Binning Determination

The fit binning is designed to optimized to ensure at least 1 predicted Monte Carlo (MC) event in each bin when scaled to the collected data POT. The fit bins must also account for detector smearing effects. In order to mitigate smearing and event migration, the reconstructed kinematics were examined to their MC truth value using only correctly identified leptons in one-dimensional kinematic slices. Since the MC provides about  $10\times$  the data statistics, the statistical uncertainty for each bin should be negligible for high statistics regions. The kinematics are scanned across their full relevant spaces in order to understand the needed width for a fit bin. The first fit bin is always defined from the kinematic maximum.

For the momentum bins, the momentum resolution is compared to MC truth. The momentum resolution is defined as

$$R(r, t) = \frac{r - t}{t},$$

where  $r$  is the reconstructed momentum and  $t$  is the true value. The momentum was scanned in finite bin widths with the mean and standard deviation of the resolution  $R$  extracted. The mean and standard deviation are used as a proxy for the true bias and true resolution, respectively. In addition, a bootstrapping algorithm was employed to understand the accuracy

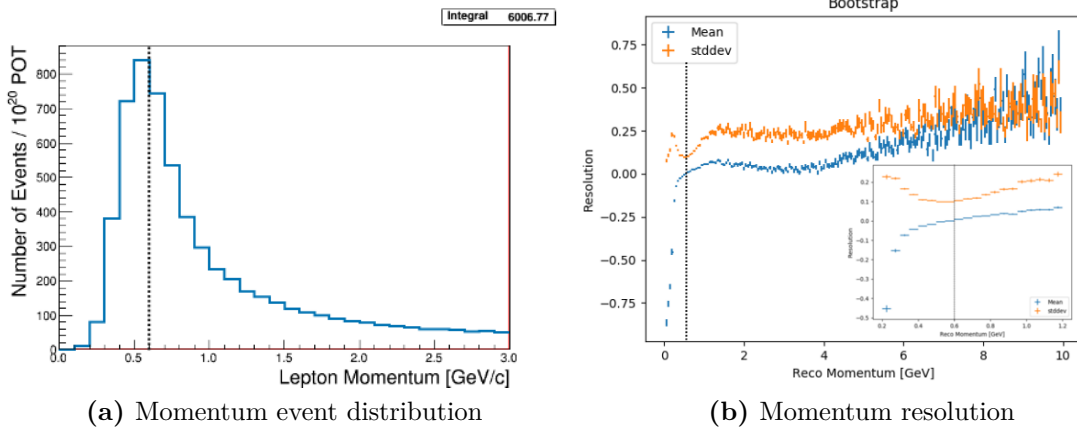


**Figure 5.1:** The momentum event distribution and uncertainty for FHC  $\nu_\mu$ CC 1-Track events is shown above. Only correctly identified muons are shown. (a) The number of events per unit momentum is scaled to  $10^{20}$  POT which is the approximate scale for all the samples in this analysis. A dashed line indicates the maximum of the peak. (b) The resolution of the momentum measurement is shown for a wide region of momenta. In the inset is the resolution zoomed near the momentum distribution maximum. Like in (a), a dashed line shows the momentum maximum.

of the sample estimates. Bootstrapping in this context is sampling over all relevant values of true momentum and randomly replacing the values. For each scanned bin, at least 1000 bootstrapping sampling with replacement was performed. In the case of large variances in the bootstrapping samples, additional 10000 sampling with replacement were performed. The results for analyzing the FHC  $\nu_\mu$ CC 1-Track selection is shown in Figure 5.1 on page 76.

The angle bins are treated in an almost identical manner. While the fit bins and physics parameterized in  $\cos \theta$ , the angle with respect to the z-axis, the detector smearing is a function of the angle  $\theta$ . In addition, since the angle can be nearly zero for the most forward-going tracks, the resolution was not used to characterize the angular uncertainties. Instead, the difference between the true and reconstructed angle were analyzed as shown in . The mean and standard deviation were studied. Bootstrapping was again used to quantify the accuracy of the mean and standard deviation.

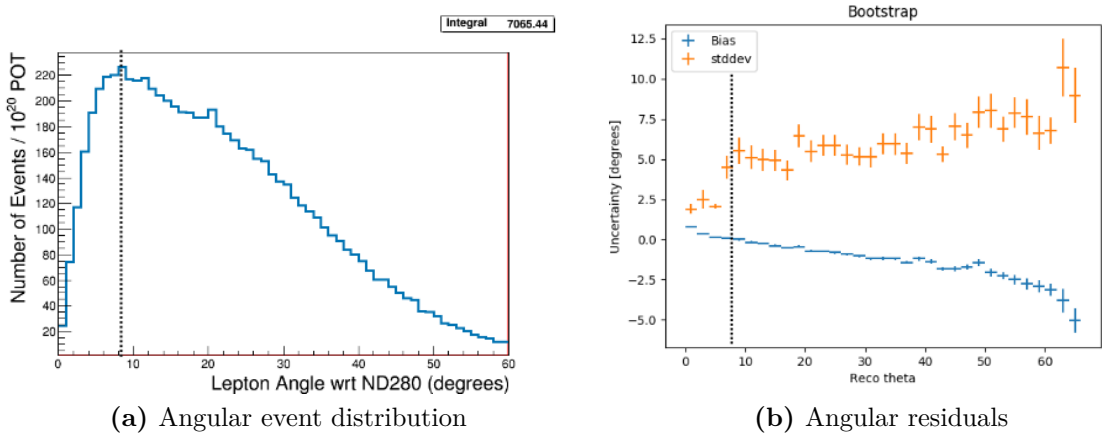


**Figure 5.2:** The angular event distribution and uncertainty for FHC  $\nu_\mu$ CC 1-Track events is shown above. Only correctly identified muons are shown. (a) The number of angular events is scaled to  $10^{20}$  POT which is the approximate scale for all the samples in this analysis. A dashed line indicates the maximum of the peak. (b) The residual of the angular measurement is shown up to where there are sufficient statistics. Like in (a), a dashed line shows the momentum maximum.

---

---

# Chapter 6

## Fitter Validation

Fitter validation

---

---

# Chapter 7

## Fitter Results

Fitter results

---

---

# Chapter 8

## PØD and FGD BANFF Comparisons

P0D-FGD comparisons

---

---

# **Chapter 9**

## **Discussion**

Discussion

# Bibliography

- [1] K. Abe et al. The T2K Experiment. *Nucl. Instrum. Meth.*, A659:106–135, 2011. 25, 28, 29, 31, 33, 37, 41, 56
- [2] K. Abe et al. Measurements of the T2K neutrino beam properties using the INGRID on-axis near detector. *Nucl. Instrum. Meth.*, A694:211 – 223, 2012. 32, 34
- [3] K. Abe et al. Observation of Electron Neutrino Appearance in a Muon Neutrino Beam. *Phys. Rev. Lett.*, 112:061802, 2014. 26
- [4] K. Abe et al. Measurement of neutrino and antineutrino oscillations by the T2K experiment including a new additional sample of  $\nu_e$  interactions at the far detector. 2017. 44
- [5] K. Abe et al. Search for CP Violation in Neutrino and Antineutrino Oscillations by the T2K Experiment with  $2.2 \times 10^{21}$  Protons on Target. *Phys. Rev. Lett.*, 121:171802, Oct 2018. 26
- [6] K. Abe and Others. Measurement of  $\nu_\mu$  and  $\bar{\nu}_\mu$  charged current inclusive cross sections and their ratio with the T2K off-axis near detector. *PHYSICAL REVIEW D*, 96(5), September 2017. 39
- [7] C. Adams et al. The Long-Baseline Neutrino Experiment: Exploring Fundamental Symmetries of the Universe. 2013. arXiv:1307.7335. 4, 22, 25

- 
- [8] Jiro Arafune, Masafumi Koike, and Joe Sato. CP violation and matter effect in long baseline neutrino oscillation experiments. *Phys. Rev. D*, 56:3093–3099, Sep 1997. 24
- [9] S. Baker and R. D. Cousins. Clarification of the use of Chi-Square and Likelihood Functions in Fits to Histograms. *Nucl. Instrum. Meth.*, A221:437–442, 1983. 48
- [10] S. Bolognesi and Others. NIWG model and uncertainties for 2017 oscillation analysis, April 2017. T2K-TN-315 v5. 53
- [11] J-PARC Center. What is J-PARC?, January 2019. <https://j-parc.jp/researcher/en/about/what/index.html>, Accessed on 26 January 2019. 27
- [12] A. Chulliat and Others. The US/UK World Magnetic Model for 2015-2020. Technical report, National Geophysical Data Center, NOAA, 2015. 35
- [13] B. T. Cleveland and Others. Measurement of the Solar Electron Neutrino Flux with the Homestake Chlorine Detector. *Astronomical Journal*, 496:505–526, March 1998. 13
- [14] R. Das and Others. Measurement of Induced Charged Current Cross Section on Water using the PØD and TPC, November 2014. T2K-TN-100. 55
- [15] A. de Gouvea et al. Working Group Report: Neutrinos. In *Proceedings, 2013 Community Summer Study on the Future of U.S. Particle Physics: Snowmass on the Mississippi*, 2013. arXiv:1310.4340. 22
- [16] I. Esteban et al. Global analysis of three-flavour neutrino oscillations: synergies and tensions in the determination of  $\theta_{23}$ ,  $\delta_{\text{CP}}$ , and the mass ordering. 2018. arXiv:1811.05487. 23
- [17] A. Ferrero. The ND280 Near Detector of the T2K Experiment. *AIP Conference Proceedings*, 1189(1):77–82, 2009. 25
- [18] J. A. Formaggio and G. P. Zeller. From eV to EeV: Neutrino Cross Sections Across Energy Scales. *Rev. Mod. Phys.*, 84:1307–1341, 2012. 45

- 
- [19] S. Fukuda et al. The Super-Kamiokande detector. *Nuclear Instruments and Methods in Physics Research Section A: Accelerators, Spectrometers, Detectors and Associated Equipment*, 501(2):418 – 462, 2003. 25
- [20] M. Hartz and Others. Constraining the Flux and Cross Section Models with Data from the ND280 Detector for the 2014/15 Oscillation Analysis, May 2015. T2K-TN-220 v4. 46, 49
- [21] A. Hillairet and Others. ND280 Reconstruction, Nov 2011. T2K-TN-72 v1. 58
- [22] Susumu Igarashi. Recent Progress of J-PARC MR Beam Commissioning and Operation. In *Proceedings, 57th ICFA Advanced Beam Dynamics Workshop on High-Intensity and High-Brightness Hadron Beams (HB2016): Malmö, Sweden, July 3-8, 2016*, page MOAM6P60, 2016. 28
- [23] C. Jarlskog. A Basis Independent Formulation of the Connection Between Quark Mass Matrices, CP Violation and Experiment,. *Z. Phys.*, C29:491–497, 1985. 22
- [24] E. Komatsu and Others. Seven-year Wilkinson Microwave Anisotropy Probe (WMAP) Observations: Cosmological Interpretation. *Astrophys. J.*, 192:18, February 2011. 24
- [25] K. Mahn and Others. Implementation of new cross section parameters for the 2017 oscillation analysis, 2017. T2K-TN-307. 53
- [26] Z Maki, M. Nakagawa, and S. Sakata. Remarks on the Unified Model of Elementary Particles. *Progr. Theor. Exp. Phys.*, 28(5), 1962. 19
- [27] B. Pontecorvo. Inverse Beta Processes and Nonconservation of Lepton Charge. *J. Exp. Theor. Phys.*, 28(5), 1957. 19
- [28] B. Pontecorvo. Mesonium and Anti-Mesonium. *Sov. Phys. JETP*, 6:429, 1957. 14

- 
- [29] P. K. Saha et al. Simulation, measurement, and mitigation of beam instability caused by the kicker impedance in the 3-GeV rapid cycling synchrotron at the Japan Proton Accelerator Research Complex. *Phys. Rev. Accel. Beams*, 21:024203, Feb 2018. 28
- [30] Andrei D Sakharov. Violation of CP invariance, C asymmetry, and baryon asymmetry of the universe. *Soviet Physics Uspekhi*, 34(5):392, 1991. 25
- [31] J. Schechter and J. W. F. Valle. Neutrinoless double- $\beta$  decay in  $SU(2) \times U(1)$  theories. *Phys. Rev. D*, 25:2951–2954, 1982. 20
- [32] N. Schmitz. *Neutrinophysik*. Teubner, Stuttgart, 1997. 18
- [33] T. Sekiguchi et al. Development and operational experience of magnetic horn system for T2K experiment. *Nuclear Instruments and Methods in Physics Research Section A: Accelerators, Spectrometers, Detectors and Associated Equipment*, 789:57 – 80, 2015. 29
- [34] M. Tanabashi et al. The Review of Particle Physics. *Phys. Rev. D*, 98(030001), 2018. 19, 23
- [35] Peter von Ballmoos. Antimatter in the Universe: constraints from gamma-ray astronomy. *Hyperfine Interactions*, 228(1):91–100, Oct 2014. 25
- [36] L. Wolfenstein. Neutrino oscillations in matter. *Phys. Rev. D*, 17:2369–2374, May 1978. 23
- [37] Y. Yamazaki, editor. *Accelerator technical design report for high-intensity proton accelerator facility project, J-PARC*. Number 2002-013. Japan Atomic Energy Research Institute, 2003. 28
- [38] Kai Zuber. *Neutrino Physics*. CRC Press, Boca Raton, FL., 2nd edition, 2012. 2, 14, 18